The film-boiling densification process for C/C composite fabrication : from local scale to overall optimization

Gerard L. Vignoles, Jean-Marc Goyhénèche, Patrick Sébastian, Jean-Rodolphe Puiggali, Jean-François Lines, Jean Lachaud, P. Delhaès, Michel Trinquecoste

THE FILM-BOILING DENSIFICATION PROCESS FOR C/C COMPOSITE FABRICATION : FROM LOCAL SCALE TO OVERALL OPTIMIZATION

Gérard L. Vignoles [a,*], Jean-Marc Goyhénèche [a],

Patrick Sébastian [b], Jean-Rodolphe Puiggali [b],

Jean-François Lines [b,a], Jean Lachaud [c,a],

Pierre Delhaès [c], and Michel Trinquecoste [c]

[a] *Laboratoire des Composites ThermoStructuraux (LCTS) ,*
UMR 5801 CNRS-CEA-Snecma-Université Bordeaux l,
3, Allée La Boëtie, F-33600 Pessac, France

[b] *TRansport, Ecoulements de FLuides, Energétique (TREFLE) ,*
UMR 8508 CNRS-ENSAM-ENSCPB-Université Bordeaux l ,
Esplanade des Arts et Métiers , F-33405 Talence Cedex, France

[c] *Centre de Recherches Paul Pascal (CRPP) ,*
UPR 8641 CNRS ,
Avenue du Dr. Schweitzer , F-33600 Pessac, France

Abstract

The film-boiling densification process is an alternative of Chemical Vapor Infiltration involving a strong thermal gradient. It allows to fabricate composite materials

starting from a fibrous preform lying in a boiling hydrocarbon precursor, the cracking of which results in a solid deposit constituting the matrix of the carbon/carbon composite. A modelling approach is presented and validated with respect to experimental data. Then, the sensitivity of the process is studied with respect to various parameters. Optimization guidelines are proposed, in conjunction with a discussion on the densification front that characterizes the process. It is thus possible to evaluate the minimal amount of power required, while maintaining the quality of the produced material, *i. e.* its bulk density and homogeneity.

Key words: Chemical processes, Composites, Materials Processing, Modelling, Optimization, Porous media

---

* to whom correspondence should be addressed
Email addresses: vinhola@lcts.u-bordeaux1.fr (Gérard L. Vignoles), goyhenec@lcts.u-bordeaux1.fr (Jean-Marc Goyhénèche), patrick.sebastian@bordeaux.ensam.fr (Patrick Sébastian), jean-rodolphe.puiggali@bordeaux.ensam.fr (Jean-Rodolphe Puiggali), jf_lines@yahoo.fr (Jean-François Lines), lachaud@lcts.u-bordeaux1.fr (Jean Lachaud), delhaes@crpp-bordeaux.cnrs.fr (Pierre Delhaès), trinquecoste@crpp-bordeaux.cnrs.fr (Michel Trinquecoste).

1 Introduction

Carbon/carbon (C/C)composite materials have thermal, mechanical and tribological properties that are particularly interesting at high temperature [Broquère et al.(1985)]; they are widely used in the fields of aerospace propulsion and aeronautical braking [Fitzer(1987)]. Various processes exist to fabricate these thermostructural composite materials [Naslain and Langlais(1986)]. In particular, starting from a fibrous preform and a precursor from which the matrix is generated by gas deposition, the process is named Chemical Vapor Infiltration [Besmann et al.(1991), Naslain and Langlais(1990)]. Its application to C/C composites is known since years, and several variants do exist [Delhaès(2003)]. The process studied here is a rapid densification process [Houdayer et al.(1984)], also named "film-boiling" process [David et al.(1999)]. It consists in holding the fibrous medium in the precursor in liquid state rather than in vapor state : even if the deposition is carried out by CVI, a strong thermal gradient is ensured by the presence of biphasic zone close to the densification zone. Thus, this process represents an extreme case of the so-called "thermal-gradient CVI" (TG-CVI) [Leutard et al.(2002)]. The high thermal gradient, associated to a higher pressure than in other variants of CVI [Houdayer et al.(1984)], allows to increase the densification rate (up to 50 times higher). However, the high energy consumed ($\approx 14\ kWh$ during 5 hours for a 30 g piece !) and the security issues linked to the use of a boiling hydrocarbon discourages the industrial scale-up of this process. Another issue is the controlability of the process, which is difficult without a sound knowledge of the intrinsic physico-chemical phenomena. The technological goals are thus :

(1) reducing the consumed power,

(2) minimizing the densification time, or at least maintaining it constant,

(3) guaranteeing the material final quality.

In this work, the only studied quality criterion is the final porosity and homogeneity of the composite ; indeed, the precise nanotexture of the obtained deposits is also an issue [Bokros(1969),Loll(1976)], but it will not be addressed here.

In order to optimize the process, a strategy based on numerical modelling has been set up. This is a commonly used method : numerous applications examples may be found in recent literature for physico-chemical multi-scale process modelling aimed at process understanding, control and optimization [Li and Christofides(2005),Okkerse et al.(2000),Dollet(2004),Boerefijn and Hounslow(2005), Ilegbusi et al.(2000)]. In a first part, a phenomenological analysis will be presented. It leads : *i*) to an identification of the couplings between the various physical and chemical phenomena, *ii*) to the evaluation and comparison of various time and space scales and *iii*) to an evaluation of the significant role played by temperature and density. The second part is devoted to the presentation of a detailed modelling strategy. Heat and species mass transport equations, featuring chemical reaction and Joule heating power supply, are solved. The modelling of resistive heating is solved separately. The third part is an analysis of the couplings, and a validation of the densification model by confrontation of numerical and experimental results. Guidelines to optimize the process are then proposed, through the identification of distinct operating zones in parameter space, depending on the existence or not of a densification front.

2 Process description and analysis

2.1 Description

In this process, the preform to be densified is settled around a resistive or inductive heating device and lies at first in a liquid carbonaceous precursor [Houdayer et al.(1984)]. Here cyclohexane has been chosen as the precursor, mainly because its boiling point at room pressure (353 K) is suitable and its molar carbon yield may be high.

The resistor allows to reach high temperatures in the center of the preform ($\approx$ 1400 K). The precursor inside the preform is then vaporized and a film-boiling zone is formed inside the hot zone (figure 1). Two layers of Goretex® textile allow to maintain the biphasic zone out of the preform, thus ensuring that the precursor is fully in vapor phase inside the densification zone. The latter is defined as the part of the hot zone in which the temperature is high enough to let the precursor cracking occur. A device located in the upper part of the apparatus condenses cyclohexane vapor and by-product gases resulting from the chemical reactions. Thus, the liquid precursor is collected for continuous re-use in the process.

2.2 Physicochemical phenomena and couplings

Previous studies on the rapid densification process [Beaugrand(2000, Bruneton et al.(1997), Rovillain et al.(2001)] pointed out the various physical and chemical phenomena involved in the preform densification. These phenomena were collected into four subsets :

(1) electrokinetics, which accounts for resistive heating,

(2) heat transfer from the power injection devices to the cold parts of the

apparatus,

(3) boiling, which includes fluid transport and phase change, and

(4) densification, which is the result of gas species transport within the preform and homogeneous and heterogeneous chemical reactions leading to pyrocarbon deposition.

The couplings between these subsets are presented on figure 2. It appears that most thermophysical parameters (thermal and electrical conductivities, specific heat, diffusion coefficients), as well as the reaction rate, depend essentially on two physical quantities : (i) temperature, and (ii) porosity ε, which translates the evolution of material structure during densification.

2.3 Space and time scales

The rapid densification process involves many elements the characteristic length scales of which have been reported at figure 3. This graph shows that the interval is broad, ranging from 10^{-6} m (pore sizes) up to 10 m for the whole apparatus and its environment.

The multi-scale modelling strategy follows the indications of figure 3. As the main goal of the study is the global process optimization, the most important issue is to provide a global-scale modelling tool. The optimization arises not only from a judicious choice of some physico-chemical parameters, but also from an appropriate design of the components. This implies the necessity to handle behavior models for all ancillary components. On the other hand, the prediction of the final quality of the material relies on the physico-chemical modelling at preform scale. Any phenomena arising at lower scales should then be treated as the result of change-of-scale methods (homogenization, asymptotic methods, etc ...), that is, laws linking between themselves parameters defined at preform scale. The elementary heterogeneous chemical

reaction has been determined in the case of single-fibre deposition experiments [Beaugrand(2000], and is considered as valid at preform scale also.

The characteristic times involved in the process are listed at figure 4. Two characteristic times are much shorter than the other ones, respectively linked to the electromagnetism and some fast (gas-phase) chemical reactions. For those two kinds of phenomena, the modelling strategy will make use of steady-state relationships.

3 Modelling strategy

A numerical modelling scheme has been set up in order to predict the time evolution of densification, using as inputs :

(1) process control parameters (power injected into the heater and reactor pressure).
(2) thermophysical data of preform, precursor and pyrocarbon.
(3) chemical deposition rate law.

Items 2 and 3 have been collected either from available literature, or from specific experimental determinations. The modelling scheme is described in the following parts.

3.1 Reaction rate and chosen species

Gas chromatography and mass balances performed on the process in a previous study [Rovillain(1999)] have lead to the following approximate overall chemical

balance :

$$C_6H_{12} \longrightarrow 1.29pyC(s) + 0.89H_2 + 0.5CH_4 + 0.15C_2H_2... \\ ... + 0.75C_2H_4 + 0.05C_2H_6 + 0.13C_3H_6 + 0.48C_4H_8 + \epsilon PAH \quad (1)$$

A full model of the complex set of heterogeneous and homogeneous reactions is out of scope of this work ; instead, it has been chosen to represent the experimental carbon balance between consumed cyclohexane and pyrocarbon and gaseous by-products by fitted stoichiometry coefficients. Also, a detailed information on the by-product gas composition is not of prime interest here. It has been chosen to lump all by-products into a single gaseous pseudo-species X ($C_{1.6}H_{4.07}$), which is designed to satisfy the experimentally determined mole and mass balances. Neglecting PAHs, this leads to the following balance :

$$C_6H12 \longrightarrow 1.29pyC(s) + 2.95C_{1.6}H_{4.07} \quad (2)$$

This allows to limit the number of computed gas species to two : this is enough to capture the essential of the process behavior, while keeping the computational time into reasonable limits. The kinetic law is of Arrhenius-Kooij type ; its parameters k_0, β and E_a were determined by an inverse method [Beaugrand(2000] from single-fibre deposition experimental results [Rovillain et al.(2001)].

3.2 Balances and laws

The proposed model takes into account heat and species transport phenomena (viscous flow, binary and Knudsen diffusion) and a homogenized heterogeneous chemical deposition reaction, which relies on the internal surface area. In the frame of the Dusty-Gas Model [Mason and Malinauskas(1983)] for multicomponent transport, the species molar fluxes J_c and J_x have a viscous and a diffusive component, the coefficient of which depends on effective binary and

Knudsen diffusion coefficients.

The balance equations which were implemented numerically in a finite elements computer code for an axisymmetric configuration are presented at Table 1, along with the associated constitutive laws. Solvers for inductive and resistive heatings have also been implemented, but we will focus here only on the resistive heating, for which accurate enough experimental data were available.

3.3 Materials properties

The considered model relies on many material properties, some of them being related to gases and other ones either to the solid or to the gas/solid composite. All thermophysical values for gases have been fitted to data from Reid et al. [Reid et al.(1987)]. Typical values for cyclohexane have been taken for most of them : indeed, since they are usually dominated by the values associated to the solid phase, there is no need to have a very precise gas-mixture description of λ and ρc. Diffusion coefficients have been evaluated with the coupled formed by C_6H_{12} and the lumped species X (see above). However, for sake of simplicity, C_2H_4 was used for the calculation of the diffusive properties of X. Note that the gas thermal conductivity and diffusivities are not pure gas-phase properties but include the effect of the porous medium geometry.

Thermophysical values for the solids (fiber, pyC deposit) have been fitted to experimental determinations by Beaugrand [Beaugrand(2000] on RVC 2000® carbon fiber felts with pyrocarbon deposits. This preform consists of 10-μm diameter ex-PAN carbon fibers in a random 3D arrangement; the average initial pore diameter being 40 μm, and the initial porosity 94%. Previous studies (*e.g.* [Rovillain et al.(2001)]) show that a final porosity indeed exists in such a material, ranging between 2 and 9 %, with an average value of 4 %. In the

following, only the open (accessible) porosity will be retained as a parameter and an extra closed porosity of 4 % is assumed. The chosen geometrical and transport parameter laws (*i.e.* internal surface area and tortuosities with respect to viscous, diffusive, and effusive transport) are relative to 3D random fiber arrangements [Sotirchos and Tomadakis(1990), Tomadakis and Sotirchos(1991b), Tomadakis and Robertson(2005)]. However, for surface area, a polynomial approximation has been chosen. It has been designed in such a way that the experimentally determined value for the raw preform $\sigma_v(\varepsilon_0)$ is respected. It has been noticed that the relation :

$$\sigma_v(\varepsilon_0) = \frac{4(1-\varepsilon_0)}{d_f} \tag{3}$$

is indeed verified up to a few percents error. A second condition for the polynomial law is that $\sigma_v \to 0$ when $\varepsilon \to 0$, and a third condition is that the slope of $\sigma_v(\varepsilon)$ is equal to $-4/d_f$, as in relation (3). The influence of the surface area law model is discussed in a later section. The necessary data for the simulation are summarized at tables 2-5.

4 Validation of the numerical procedure

4.1 Experimental configuration

In order to validate the numerical model, a confrontation with experimental data [Delhaès et al.(2005)] has been carried out. The selected configuration featured an RVC 2000® preform (height = 90 mm, outer diameter = 50 mm and inner diameter = 20 mm). The preform was surrounded by two layers of 0.3 mm thick Goretex ® fabric. These have the effect of ensuring that the interior of the preform is exclusively filled with vapor, while maintaining the biphasic domain in close contact with the device during most of the run. Temperature on the internal face of the preform has been maintained at

1373 K; and the densification has been carried out at atmospheric pressure. The thermal gradient time evolution has been recorded by six thermocouples [Delhaès et al.(2005)]. It has been checked by a 3D thermal computation that the thermocouples do not introduce a significant bias in the temperature field. The domain geometry and boundary conditions are sketched at figure 5. The evolutions of power supply within the preform and of the coupling between electrical and thermal phenomena during densification have also been studied. As a matter of fact, the choice of an RVC 2000® preform is not optimal in terms of composite material quality ; other fibrous architectures, like Novoltex® [Delhaès et al.(2005)] could be more suitable; however RVC 2000® felt is a simple enough porous medium for convenient studies on the process.

4.2 Coupling between "thermal transport" and "heat supply" models

The influence of densification on the distribution of heating power density is presented at figure 6. At the beginning, porosity is high (94 %) and the preform has a low electrical conductivity; consequently, the power is localized only inside the resistor. However, the pyrocarbon deposited during densification has a high electrical conductivity; so, the equivalent conductivity of the preform reaches the same order of magnitude as that of the graphite resistor. It is shown that 30 % of the power is dissipated inside the perform itself. In such a situation, the thermal gradient is lowered and the composite quality gets affected; consequently, it has been decided to insulate electrically the resistor. It then becomes possible to model the energy contribution by a flux imposed on the internal face of the preform, and thus to avoid electrokinetic equation solving.

4.3 Coupling between " thermal " and " densification " subsets : validation on thermal data

Figure 7 presents a satisfactory agreement between measured and calculated thermal profiles from the beginning of the experience to at least 2 h of densification. This brings a sound experimental validation to the model. However, at 5 h of densification, a marked change of the thermal gradient arises and is not reproduced by the model [Lines et al.(2005)]. This can be explained by the fact that the film-boiling zone is not any more confined close to the perform outer boundary : the whole preform is now surrounded by a continuous gaseous film. Such a situation lowers by several orders of magnitude the boundary heat exchange coefficient, and alters appreciably the thermal behaviour of the process : indeed, the thermal gradient is strongly hampered, and it is an adverse effect for the material quality, as will be seen in the following parts. Also, the process security is not guaranteed any more, and the power has to be shut down at that moment. It would be an easy task to account for overall calefaction in the model through the use of a different BC at the preform/fluid interface ; this has not been made since the phenomenon occurs only at the end of the cycle, and has no practical consequence on the produced piece (it is reshaped before use).

During most of the processing run, three zones are neatly distinguished. A first zone, where the average thermal gradient is around 30 $K.mm^{-1}$ (after 2 h of densification), lies close the heating resistor. In the outer zone, the gradient can reach several hundreds of $K.mm^{-1}$. These two zones correspond respectively to :

- (i) the densified zone, which is a correct thermal conductor ($\lambda \approx 9\, W.m^{-1}.K^{-1}$) and
- (ii) the crude preform, the conductivity of which is much lower ($\lambda \approx 0.1$

$W.m^{-1}.K^{-1}$).

The presence of this gradient contrast helps to locate the radial position of the third zone, which is the densification front. This narrow zone is the only one where deposition reactions are active. It had already been evidenced in thermal-gradient CVI [Melkote and Jensen(1990),Leutard et al.(2002)], but is more markedly present in the present process because of the extreme importance of the thermal gradient.

One of the easiest ways to validate the model is to locate the front position from the thermal profile. Also, density-based methods have also been used in order to double-check the results and validation.

4.4 Model validation by density assessment

Various methods may be used for the assessment of density inside the preform :

- (*i*) Deposit thickness measurements on lone fibers
- (*ii*) X-ray radiographs
- (*iii*) X-ray tomographs.

Of these, the last two are non-destructive. All have been employed, and the results are compared between themselves, and to the numerical predictions.

4.4.1 Deposit thickness measurements

An optical microscope is used to measure directly the deposit thickness around fibers on a polished section of the material, as in figure 8a. The thickness is plotted against the radial position of the fibers. Figure 8b is an example of such a plot, taken in radial direction at half-height. The predicted front position and width match correctly the experimental determination : this provides a rapid 1D validation of the numerical procedure. However, it is a rather tedious

method for a validation in 2D ; this is why X-ray based methods have been also considered.

4.4.2 X-ray radiographs

This method, of simple implementation, allows to get density measurements from horizontal or vertical projections. Also, vertical (respectively, horizontal) projections have been used principally to check the radial (respectively, axial) position of the thermocouples. Figure 9 is an example : the positions have been determined with a precision of $\pm$ 0.25 mm, which is fairly enough for our purpose.

The densification profiles are obtained indirectly from the horizontal radiographs. Indeed, the absorption path lengths are larger at the preform center than in tangency to the outer radius. This phenomenon, inherent to the radiography principle, is taken into account by the use of Abel transform. Such a transform, upon the hypothesis of axial symmetry, allows to retrieve an estimation of radial density profiles from the projection. The raw images have been discretized in pixels with greyscale levels, and the transform applied to each pixel row. The result is scaled with the knowledge of two density values : the graphite tube density and the raw preform density. Such an indirect tool has some limits. First, the hypothesis of axial symmetry is not totally respected in the experiment ; second, some X-ray hardening is present since a classical polychromatic source is used ; third, the hypothesis of linearity of the gray-levels scale may be violated due to detector saturation effects. Figure 10 shows a comparison between raw X-ray absorption, Abel-transformed X-ray signal, and numerical simulation. It is clear that the use of the Abel transform allows to locate more clearly the front position, although some X-ray hardening is present.

4.4.3 X-ray tomographs

This method is based on the same principle as the preceding one, but now many radiographs are taken at various angular positions; the 3D object is then reconstructed numerically, usually by filtered backprojection [Kak and Slaney(2001)]. In our case, a vertical slice of the reconstruction is enough for density assessment, still under the hypothesis of cylindrical symmetry. Calibration has been performed with the use of some plugs of known density settled close to the preform. Figure 11 shows an excellent agreement between computed and imaged density fields after 2 hours of processing time.

4.4.4 Choice of a method and assessment

Among the presented methods, the X-ray radiography with Abel transform has been selected because it is cheap, non-destructive, and fast. Figure 12 is a comparison of X-ray data with numerical results at 30 min, 2, 3 and 5 h of processing. The radial position of the front is satisfactorily described by the model at all times. Moreover, a fair agreement is also obtained on the 2D "barrel-like" repartition of density. Accordingly, it may be concluded that the model has been validated against experimental results and is able to predict the evolution of density with time.

4.5 Power history and energy balance

In addition to thermal profiles or density profiles, the consumed power has been monitored during the experimental runs. The model is able to provide estimates of the power that traverses the preform, which is somewhat inferior to the total power since some heat is transferred directly from the resistor to the surrounding fluid. An interesting point is that the power always increases during process operation, due to the increase in overall thermal conductivity

while the temperature difference is maintained constant. Indeed, the power increase is a sign of the process advancement.

The experimental laboratory-scale setup has been studied on the point of view of energy balance [Courault(1995), Delhaès et al.(2005), Lachaud(2002)]. The input power is entirely transmitted to the system by Joule effect, and ranges between 0.7 and 2 kW from the beginning to the end of processing. However, some part of it is lost by direct transmission of heat from the extremities of the set-up holders (located above and below the preform) to the surrounding fluid. The remaining power helps to construct the thermal gradient, and will be called "efficient" power . The total power output arises from three main factors :

— Radiation and convection towards room temperature. Its value is considered roughly constant throughout the process.
— Heat transferred to the condenser.
— The chemical deposition reaction.

More rigorously, one has also to take into account the power loss associated to the evacuation of the non-condensable by-products (mainly CH_4 and H_2), but since their specific heat is low, this contribution is negligible.

The numerical simulation provides estimates of the "efficient" power, as a function of time. This can be compared to the total electrical power injected into the system, in order to recover the side losses. Also, the chemical reaction energy consumption is evaluated by the computation of the reaction molar enthalpy $\Delta_r H(T)$ using the stoichiometric coefficients of equation (1) and thermochemical data [Reid et al.(1987)]. Actually, it is verified that it represents a small amount of the total input power : at most 45 W, that is, less than 3 %, and it decreases after 1 h of processing time. Using the simulation results, power history graphs have been built, and are shown in figure 13. It is seen that the "non-efficient" power is remarkably constant – indeed, this

was to be expected, since it corresponds to the heat transferred by the sample holders to the boiling fluid. Accordingly, the total power increase is quite equal to the efficient power increase, that the model has managed to capture. Also, the power output decomposition yields a roughly constant term linked to radiative and convective losses towards the surrounding ; the total power variation is approximately equal to the power received by the condenser. However, there is no precise relationship between the "efficient" power and the power received by the condenser.

5 Model sensitivity study

Once the model has been validated, it is of interest to test its sensitivity to some internal parameters, in order to assess its level of confidence, and to identify what are the laws that have to be identified with most care. We will focus on transport and reaction parameters associated to the preform, namely, its thermal conductivity, its internal surface area, and the effective mass transport coefficients.

5.1 Thermal conductivity

The simulations of the validated case have been run again with solid-phase conductivity multiplied by two and divided by two (actually, the total effective conductivity is mainly due to the solid phase). Figure 14 and table 7 show that the impact on the porosity gradient and on the densification velocity is small (approximately plus or minus 10%). This was to be expected since the process works with imposed temperatures at the preform boundary. What is affected indeed is the amount of heat flux that runs across the preform, and thus the total power consumed.

5.2 Internal surface area

In addition to the reference case, several laws for $\sigma_v = f(\varepsilon)$ have been tested. They are listed at table 8 and sketched at figure 15.

Law ♯2 is a classical estimation for random overlapping cylinders [Tomadakis and Sotirchos(1991a)]; law ♯3 is a more elaborate expression taking into account the presence of a "hard-core" porosity, *i. e.* a porosity above which there is no fiber overlap [Rikvold and Stell(1985)]. They have similar properties close to ε_0 but they tend to zero in a very different way compared to law ♯1 : $\sigma_v \propto \varepsilon \ln \varepsilon$ instead of $\sigma_v \propto \varepsilon$. Law ♯4 is the same as law ♯1 but with a half slope at ε_0. Law ♯5 is a modified surface area law that matches closely the 3D random fiber model at high porosities but behaves like a random distribution of small round pores at low porosities. Again, it has been scaled such that the initial slope is $-4/d_f$. The behavior close to zero is $\sigma_v \propto \varepsilon^{2/3}$, typical of non-overlapping spherical pores.

Figure 16 is a plot of the densification profiles after 1 hour of processing, using the various laws, and figure 17 is a plot of the effect of multiplying or dividing by two the surface area law ♯1. Table 9 gives the influence of the various laws on the front position and width, and on the consumed power at 1 hour of processing time. The rightmost column of table 9 is an estimation of the scaled average surface area :

$$\overline{\sigma}_v d_f = \frac{d_f}{\varepsilon_0} \int_0^{\varepsilon_0} \sigma_v(\varepsilon) \mathrm{d}\varepsilon \tag{4}$$

First, it appears that laws ♯ 2,3,4, and 5 give position results which are lower, but relatively close to the base case. However, laws ♯ 2 and 3 display a different front shape, with a singular point at low porosities and a lesser width. Associated to this, the CPU time for the numerical resolution is multiplied by a factor 150 for these laws with respect to the other ones. Law ♯ 5 does not

display this severe drawback. On the other hand, law ♯ 4 gives a much larger front width.

Figure 17 shows the rather strong effect of the surface area scale factor (*i.e.* $4/d_f$). When it is doubled (that is, taking the half of the initial fiber diameter), then the front velocity is increased by 1/3, while the power increase is only by 1/5. Symmetrically, when the fiber diameter is doubled, then the velocity is decreased and the power decrease is again lesser than the velocity decrease. Indeed, the actual power values are essentially linked to the position of the front, which determines the thickness of the most thermally resistive part of the preform. On the other hand, there is quite no influence at all of this parameter variation on the front thickness. Also, when the law scale factor is doubled, there appears a neat residual *open* porosity, which is a severely adverse phenomenon for material quality. This will be discussed in section 6.

It is rather interesting to see that laws with similar *average* surface areas yield strongly different front behaviors. For instance, law ♯ 4 and law ♯ 1 divided by two have very similar average values, but the former gives a much faster and broader front. Also, law ♯ 3 and law ♯ 1 multiplied by two have rather comparable averages, but the latter gives a faster front. Finally, laws ♯ 2 and ♯ 3 have neatly different averages, but the resulting fronts are similar. Summarizing these comparisons, it seems that :

- the scale parameter $4/d_f$ is of highest influence on front velocity ;
- the precise way with which the specific area tends to zero when ε goes to zero is also a determining criterion for front velocity ;
- the shape of the front relies on the shape of the $\sigma_v(\varepsilon)$ law.

5.3 Influence of species mass transport terms

In the full model, three transport modalities are considered for the gas species : viscous transport (via a Darcy law), plain diffusion and Knudsen diffusion [Ofori and Sotirchos(1996)]. The relative importance of these terms is studied first, then a study of the influence of the magnitude of mass transport is given.

5.3.1 Relative influence of the transport modes

Three simulation runs have been compared : the first one contains all terms, the second one does not include Knudsen diffusion, and the last one does not include viscous transport. Figure 18 shows clearly on porosity profiles after 1 hour that if Knudsen flow is of limited influence, viscous flow has a yet smaller effect. This can be anticipated by evaluation of dimensionless groups $Kn = D_{cx}/D_{c,K}$ and $Ke_1 \approx \mu^* D_{cx}/(pK)$ [Kerkhof(1997)]. The Knudsen number is appreciable only in the region where the pores are already well densified, that is, in the few last fractions of millimeter of the densification front while the Ke_1 number is of order 10^{-4} throughout the zone where gases circulate.

As a consequence, a simplified model with a modified diffusion coefficient would be enough to describe correctly the transport of reactant gas.

5.3.2 Influence of the magnitude of transport

By dividing or multiplying by two the magnitude of the transport coefficients, it is shown that not only the front velocity, but also its shape, may be affected, as can be seen in figure 19. With a slower diffusion coefficient, the front is broader and there appears some residual porosity behind it. Clearly, in this case, the limitation by mass transfer becomes so important that there is a transition towards a situation where the densification front does not always exist ; this will be discussed in more details in section 6.

6 Process optimization

6.1 Power distribution

The analysis of the power distribution has shown that in the lab-scale process, close to half of the power is lost by direct transmission of heat from the flasks to the surrounding fluid. This suggest strongly to improve the thermal insulation of the flasks. Also, it is noticed that the transposition to industrial scale may reduce these power losses, because in a larger set-up the flask/preform contact area ratio will be smaller.

The second issue is then : is the "effective" power not too high for our needs ? in other words, is the thermal gradient not too strong ? Is it possible to lower it and still maintain the material's quality ? A parameter variation study has been performed to answer this question and is reported in the following part.

6.2 Operating zones as a function of the thermal gradient

A typical 1D process simulation run has been taken as a base case, and has then been repeated with a variation of the cold-side temperature from the precursor boiling point (for which the gradient is maximal) to the susceptor temperature (for which the gradient is zero). Figure 20 is a plot of the computed mass of pyrocarbon deposited after 5 h of densification, and of the maximal residual porosity. Figure 21 gives the porosity profiles in the three typical densification regimes that are distinguished :

- Regime 1, obtained for the highest thermal gradients, is characterized by a very low residual porosity. The deposition rate increases when the gradient decreases.
- Regime 2, for which the residual porosity is not any more negligible. The

deposition rate still increases as the thermal gradient decreases.

- Regime 3, for weak gradients, is similar to Isothermal CVI with strong diffusional limitations.

The second regime has been many times described in the case of several Thermal-Gradient CVI alternatives : F-CVI [Vaidyaraman et al.(1996)], "rapid process" [Golecki et al.(1996)], Micro-Wave CVI [Gupta and Evans(1991)], Radio-Frequency heating CVI [Morell et al.(1992), Leutard et al.(2002)]. Another illustration is given in figure 17 with a large surface area factor and in figure 19 with the curve obtained with a small diffusion coefficient, which display residual open porosity.

It is possible to understand these three regimes using the notion of densification front [Melkote and Jensen(1990), Vignoles et al.(2005)]. Indeed, if the temperature gradient is strong enough, a front settles with velocity v_{front} and width l_{front}. In regime 1, the front is present throughout the process history : the maximal densification is thus ensured. In regime 3, the temperature gradient is never sufficient to give birth to a front. The intermediate regime 2 is a situation where the gradient is initially too low (like in regime 3), but eventually increases up to a critical value above which the front appears and the regime 1 behavior is recovered.

6.3 Discussion of the front characteristics

In this section it will be tried to give a physical justification for the results of the previous section, and provide a broader information on parameter dependence of the front characteristic values, namely its width and velocity, as well as its existence.

6.3.1 Dependence to the heat flux

It has been shown [Rovillain et al.(2001)] that the velocity is approximated by the following formula (neglecting the T^β term in the Arrhenius-Kooij expression) :

$$v_{\text{front}} = (V_m \frac{p_c}{\mathcal{R}T}) \frac{2k_0}{e\|\nabla T\|} \int_{T_{min}}^{T_{max}} \exp\left(-\frac{E_a}{\mathcal{R}T}\right) \mathrm{d}T \tag{5}$$

where e is an equivalent distance between fibers in the felt, roughly equal to $4\varepsilon_0\sigma_{v,0}^{-1}$, $\|\nabla T\|$ is an average thermal gradient through the front, and $(T_{min}; T_{max})$ defines the temperature range in which the reaction occurs. Indeed, T_{min} may be viewed as an ignition temperature (below which chemical reaction is negligible) and T_{max} is the temperature at which total pore plugging or reactant consumption occurs. Expanding the integral in eq. (5) for small values of $\mathcal{R}T/E_a$, and neglecting all terms in $\exp(-E_a/\mathcal{R}T_{min})$ gives a more tractable approximation :

$$v_{\text{front}} = (V_m \frac{p_c}{\mathcal{R}T_{min}}) \left(\frac{\sigma_{v,0}\overline{\lambda}\mathcal{R}T_{max}^2}{2\varepsilon_0 E_a q}\right) \cdot k_0 \exp\left(-\frac{E_a}{\mathcal{R}T_{max}}\right) \tag{6}$$

where a front-average conductivity $\overline{\lambda}$ has been defined and q is the traversing heat flux. Also, an elementary mass balance argument shows that the reactant mole flux is roughly equal to :

$$J_c = V_m^{-1} v_{\text{front}} \approx R(T_{max}) \cdot l_{\text{front}} \tag{7}$$

From this relation and eq. (6), and noting that $J_c \approx -V_m^{-1} v_{\text{front}}$, the front width may be estimated as :

$$l_{\text{front}} \approx \frac{\overline{\lambda}\mathcal{R}T_{max}^2}{2\varepsilon_0 E_a q} \tag{8}$$

, that is, in other words, a natural length scale for thermal conduction $L_{th} = \frac{\overline{\lambda}T_{max}}{2\varepsilon_0 q}$, divided by the dimensionless activation energy $\gamma = E_a/\mathcal{R}T_{max}$. The important feature of eqs. (6) and (8) is that the front velocity and width decrease with increasing heat flux. This is exactly what happens during the process, when the hot-side temperature is maintained constant. Fig. (22) is a

plot of the computed front velocity and width as a function of time during one typical run. The temperature is held close to the precursor boiling point at the preform outer boundary, while the increase in conductivity close to the susceptor, maintained at a constant temperature, leads to an increase of the heat flux at any point inside the preform. On the other hand, the temperature at the hot side of the front decreases moderately as the front progresses. However, it is the $1/q$ behavior predicted by eqs. (6) and (8) that dominates, as illustrated by figure 22.

6.3.2 Front existence

From the preceding relations it is possible to work out an existence criterion based on a physical argument. More elaborate mathematical arguments will be presented in another paper. A necessary condition for the front existence is that the diffusive flux of reactant *through the front* $J_{c,int}$ is enough to feed the reaction zone :

$$J_{c,int} > V_m^{-1} v_{\text{front}} \tag{9}$$

This flux may be approximated by :

$$J_{c,int} \approx \overline{D_c} \frac{p_c}{\mathcal{R} T_{\text{front}}} \frac{1}{l_{\text{front}}} \tag{10}$$

where $\overline{D_c}$ and T_{front} are front-average quantities of the effective reactant diffusivity and of the temperature.

Combining together eqs. (6-10) yields an upper bound for the Thiele modulus Φ based on the front width as a reference length :

$$\Phi^2 = l_{\text{front}}^2 \frac{\sigma_{v,0} k(T_{max})}{\overline{D}} \lesssim 1 \tag{11}$$

This illustrates that the fundamental issue in the densification front is a diffusion/reaction competition. The criterion may be rewritten as a lower bound

for the heat flux [Vignoles et al.(2005)] :

$$q \gtrsim \frac{\overline{\lambda}\mathcal{R}T_{max}^2}{E_a}\sqrt{\frac{\sigma_{v,0}k(T_{max})}{\overline{D}}} \tag{12}$$

This meets the numerical and experimental evidence that a minimal heat flux is required in order to obtain a front.

6.4 Optimization guidelines

It is now possible to propose practical rules in order to optimize the process, making use of the conclusions of sections 6.2 and 6.3.

There is an optimal value of the temperature gradient, close to the limit between areas 1 and 2 in figure 20, such that the quality (*i.e.* minimal porosity) of the material is preserved, while the heat flux is as low as possible (in order to lower the power consumption), and the deposition rate is as high as possible (in order to lower the processing time). Complete material quality preservation leads only to a 30% increase in densification time compared to the fastest situation possible (limit between zones 2 and 3). Choosing this critical value of the gradient is the same as fulfilling criterion (12). From this formula, it is readily seen that this critical flux decreases when :

(1) the activation energy increases,
(2) the solid phase conductivity decreases,
(3) the initial fiber diameter increases (since $\sigma_{v,0} \approx 4/d_f$) [Vaidyaraman et al.(1996)],
(4) the gas diffusion coefficient increases (*e.g.* with a pressure decrease unless a Knudsen regime is attained),
(5) the hot side temperature decreases.

Items 1 to 3 are purely dictated by the material and precursor choices, while item 4 and 5 may be managed through process controls. Unfortunately, when

either pressure or hot-side temperature are decreased, one can use a lower heat flux (resulting in a power saving), but the front velocity decreases in a stronger fashion : this makes the processing time increase, and no energy saving is obtained in this way.

On the other hand, increasing pressure would enhance in a linear fashion the front velocity, while the critical heat flux would increase in a square-root dependence : this suggest to work at the highest possible pressures. However, working under high pressure has the severe drawback to render the setup more expensive, because of new ancillary components and extra security issues.

In practice, increasing the cold-side temperature – as suggested by figure 20 – is one of the solutions of interest : this has however the effect of transforming the "film-boiling" process into a regular TG-CVI process, because the precursor temperature at the preform boundary is not any more equal to its boiling point : this "mixed" situation has been experimented [Delhaès et al.(2003)].

The actual process contains a thermal regulation loop such that the susceptor temperature is held constant : as shown previously, this has the effect of continuously lowering the front velocity, because the heat flux increases and because the hot-side temperature decreases. This suggests that if the susceptor temperature is regulated in such a way that the heat flux suffers a lesser increase, or that the hot-side temperature is held constant, then there would be a less pronounced velocity decrease. This would shorten the densification time and the total energy consumed.

Items 2 and 3 of the discussion have been illustrated when performing experiments with Novoltex ® preforms instead of RVC2000 ® felts [Delhaès et al.(2005)]. These preforms are made of more conductive fibers, with a higher initial density and internal surface area. It has been observed that the front width was always larger, and that its existence was more difficult to obtain, a fact that can be deduced from eqs. (8) and (12).

7 Conclusions

The film-boiling CVI process features many physical and chemical phenomena which were identified and collected in a phenomenological analysis and a study of time and space scales. A numerical modelling of the electric, thermal, diffusive and reactive phenomena has been set up in order to study the influence of the medium alteration by densification on the respective couplings of heat transfer with the electric heating device and the deposition chemistry. The numerical approach has been validated against experimental thermal data. Then, optimization guidelines have been proposed for the process, based on a numerical parameter variation study. In association with this parametric study, a discussion on the existence and characteristic quantities of the densification front helps to better understand the underlying competition between transfer and chemical deposition, and to provide estimates for the minimal heat flux that ensures full densification. Other processes involving CVI with thermal gradients may be thus compared to the film-boiling process.

Future work in the modelling of this process will be a more accurate representation of some physico-chemical phenomena, among which the biphasic fluid transport and phase change, which would be necessary to extend the model to configurations where the boiling front lies inside the preform. Also, it is of great interest to use more systematic optimization tools (see *e.g.* [Bendersky and Christofides(2000)], [Choo et al.(2004)]) to precisely compute optimal process designs and operating conditions.

Acknowledgements

The authors wish to thank V. Lucas (CRPP, CNRS, Pessac, France) for experimental data and S. Beaugrand, P. David, and C. Gachet (CEA-LR, Tours, France) for many helpful discussions. This work was supported by CEA and

CNRS through a Ph.D. Grant to J.-F. Lines.

References

[Beaugrand(2000] Beaugrand, S., 2000. Etude du procédé de densification rapide par caléfaction pour l'élaboration de composites carbone-carbone. Ph.D. thesis, University of Orléans, France.

[Bendersky and Christofides(2000)] Bendersky, E., Christofides, P. D., 2000. Optimization of transport-reaction processes using nonlinear model reduction. Chem. Eng. Sci. 55, 4349–4366.

[Besmann et al.(1991)] Besmann, T. M., Sheldon, B. W., Lowden, R. A., Stinton, D. P., 1991. Vapor-phase fabrication and properties of continuous-filament ceramic composites. Science 253, 1104–1109.

[Boerefijn and Hounslow(2005)] Boerefijn, R., Hounslow, M., 2005. Studies of fluid bed granulation in an industrial R&D context. Chem. Eng. Sci. 60, 3879–3890.

[Bokros(1969)] Bokros, J. C., 1969. Deposition, structure and properties of pyrolytic carbon. Vol. 5 of Chemistry and Physics of Carbon. M. Dekker, New York, Ch. 1, pp. 1–118.

[Broquère et al.(1985)] Broquère, B. H., Buttazoni, B., Choury, J.-J., 1985. Les composites carbone/carbone. Leurs applications industrielles. In: Naslain, R. (Ed.), Introduction aux matériaux composites. CNRS and IMC, Paris, pp. 405–438.

[Bruneton et al.(1997)] Bruneton, E., Narcy, B., Oberlin, A., 1997. Carbon-carbon composites prepared by a rapid densification process. Carbon 35 (10-11), 1593–1611.

[Choo et al.(2004)] Choo, S., Lei, W., Melvin, A., Rubloff, G. W., 2004. Dynamic simulation and optimization of Cu CVD unit process for environmentally benign manufacturing. IEEE Trans. on Semicond. Manufact. 17 (3), 455–469.

[Courault(1995)] Courault, A. C., 1995. Procédé de densification rapide. Master's thesis, Université de Paris VI.

[David et al.(1999)] David, P., Benazet, J.-D., Ravel, F., 1999. Rapid deposition of carbon and ceramic matrices by film-boiling technique. In: Vicenzini, P. (Ed.), Advanced structural fiber composites. CIMTEC Procs. Techna, Faenza, Italy, pp. 135–140.

[Delhaès(2003)] Delhaès, P., 2003. Chemical vapor deposition and infiltration processes of carbon materials. Carbon 40 (5), 641–657.

[Delhaès et al.(2003)] Delhaès, P., Trinquecoste, M., Derré, A., Rovillain, D., David, P., 2003. Film boiling chemical vapor infiltration of C/C composites : Influence of mass and thermal transfers. Carbon Science 4 (4), 163–167.

[Delhaès et al.(2005)] Delhaès, P., Trinquecoste, M., Lines, J.-F., Cosculluela, A., Goyhénèche, J.-M., Couzi, M., 2005. Chemical vapor infiltration of C/C composites : Fast densification processes and matrix characterizations. Carbon 43, 681–691.

[Dollet(2004)] Dollet, A., 2004. Multiscale modeling of CVD film growth - A review of recent works. Surf. Coat. Technol. 177-178, 245–251.

[Fitzer(1987)] Fitzer, E., 1987. The future of carbon/carbon composites. Carbon 25, 163–190.

[Golecki et al.(1996)] Golecki, I., Morris, R. C., Narasimhan, D., Clements, N., 1996. Carbon-carbon composites inductively-heated and rapidly densified by thermal-gradient chemical vapor infiltration : Density distributions and densification mechanism. In: Logan, K. V., Munir, Z. A., Spriggs, R. M. (Eds.), Advanced Synthesis and Processing of Composites and Advanced Ceramics II. Vol. 79 of Ceram. Trans. The American Ceramic Society, Westerville, OH, pp. 135–142.

[Gupta and Evans(1991)] Gupta, D., Evans, J. W., 1991. A mathematical model for CVI with microwave heating and external cooling. J. Mat. Res. 6, 810–818.

[Houdayer et al.(1984)] Houdayer, M., Spitz, J., Van, D. T., 1984. US Patent no. 4 472 454.

[Ilegbusi et al.(2000)] Ilegbusi, O. J., Iguchi, M., Wahnsiedler, W., 2000. Mathematical and Physical Modelling of Materials Processing Operations. Vol. 9 of CRC Mechanical Engineering Series. Chapman and Hall / CRC, Boca Raton, FL, USA.

[Kak and Slaney(2001)] Kak, A. C., Slaney, M., 2001. Principles of computerized tomographic imaging. Vol. 33 of Classics in Applied Mathematics. SIAM.

[Kerkhof(1997)] Kerkhof, P. J. A. M., 1997. New light on some old problems : Revisiting the Stefan tube, Graham's law, and the Bosanquet equation. Ind. Eng. Chem. Res. 36, 915–922.

[Lachaud(2002)] Lachaud, J., 2002. Procédé de densification rapide "Kalamazoo" : Validation expérimentale pour une modélisation. technical report, ENSAM-CRPP, Bordeaux.

[Leutard et al.(2002)] Leutard, D., Vignoles, G. L., Lamouroux, F., Bernard, B., 2002. Monitoring density and temperature in C/C composites elaborated by CVI with radio-frequency heating. J. Mater. Synth. and Proc. 9 (5), 259–273.

[Li and Christofides(2005)] Li, M., Christofides, P. D., 2005. Multiscale modeling and analysis of an industrial HVOF thermal spray process. Chem. Eng. Sci. 60, 3649–3669.

[Lines et al.(2005)] Lines, J.-F., Vignoles, G. L., Goyhénèche, J.-M., Puiggali, J.-R., 2005. Thermal modelling of a carbon/carbon composite material fabrication. In: Denis, S. (Ed.), Proc. Intl. Conf. on Thermal Process Modelling and Computer Simulation 2003. J. Phys. IV France. EDP Sciences, Les Ulis, France, to appear.

[Loll(1976)] Loll, P., 1976. Préparation et propriétés physiques de composites carbone/carbone déposés en phase vapeur. Ph.D. thesis, Université Bordeaux 1 n° 240.

[Mason and Malinauskas(1983)] Mason, E. A., Malinauskas, A. P., 1983. Gas transport in porous media: the Dusty-Gas Model. Chemical engineering monographs. Elsevier.

[Melkote and Jensen(1990)] Melkote, R. R., Jensen, K. F., 1990. A model for chemical vapor infiltration of fibrous substrates. In: Besmann, T. M., Gallois, B. M. (Eds.), Chemical Vapor Deposition of Refractory Metals and Ceramics. Vol. 168 of Mat. Res. Soc. Symp. Proc. Materials research Society, Pittsburgh, Pennsylvania, pp. 67–72.

[Morell et al.(1992)] Morell, J. I., Economou, D. J., Amundson, N. R., 1992. Pulsed-power volume-heating chemical vapor infiltration. J. Mater. Res. 7, 2447–2457.

[Naslain and Langlais(1986)] Naslain, R., Langlais, F., 1986. CVD-processing of ceramic-ceramic composite materials. In: Tressler, R., Messing, G., Pantano, C., Newnham, R. (Eds.), Tailoring multiphase and composite ceramics. Vol. 20 of Mat. Sci. Res. Kluwer Acad. Pub., Dordrecht, The Netherlands, pp. 145–164.

[Naslain and Langlais(1990)] Naslain, R., Langlais, F., 1990. Fundamental and practical aspects of the chemical vapor infiltration of porous substrates. High Temperature Science 27, 221–235.

[Ofori and Sotirchos(1996)] Ofori, J. Y., Sotirchos, S. V., 1996. Multicomponent mass transport in CVI. Ind. Eng. Chem. Res. 35, 1275.

[Okkerse et al.(2000)] Okkerse, M., Kleijn, C. R., van den Akker, H. E. A., de Croon, M., Marin, G. B., 2000. Two-dimensional simulation of an oxy-acetylene torch diamond reactor with a detailed gas-phase and surface mechanism. J. Appl. Phys. 88, 4417–4428.

[Reid et al.(1987)] Reid, R. C., Prausnitz, J. M., Poling, B. E., 1987. The properties of gases and liquids, 4th Edition. McGraw Hill Book Company.

[Rikvold and Stell(1985)] Rikvold, P. A., Stell, G., 1985. Porosity and specific surface for interpenetrable-sphere models of two-phase random media. J. Chem. Phys. 31, 1014–1020.

[Rovillain(1999)] Rovillain, D., 1999. Procédé de densification rapide et caractérisation de composites carbone/carbone. Ph.D. thesis, Université Bordeaux 1 no. 2067.

[Rovillain et al.(2001)] Rovillain, D., Trinquecoste, M., Bruneton, E., Derré, A., David, P., Delhaès, P., 2001. Film-boiling chemical vapor infiltration. An experimental study on carbon/carbon composites. Carbon 39 (9), 1355–1365.

[Sotirchos and Tomadakis(1990)] Sotirchos, S. V., Tomadakis, M. M., 1990. Modeling transport, reaction and pore structure evolution during densification of cellular or fibrous structure. In: Besmann, T. M., Gallois, B. M. (Eds.), Chemical Vapor Deposition of Refractory Metals and Ceramics. Vol. 168 of Mat. Res. Soc. Symp. Proc. Materials research Society, Pittsburgh, Pennsylvania, pp. 73–78.

[Tomadakis and Robertson(2005)] Tomadakis, M. M., Robertson, T. J., 2005. Viscous permeability of random fiber structures : comparison of electrical and diffusional estimates with experimental and analytical results. J. Composite Mater. 39 (2), 163–188.

[Tomadakis and Sotirchos(1991a)] Tomadakis, M. M., Sotirchos, S. V., 1991a. Effective Knudsen diffusivities in structures of randomly overlapping fibers. AIChE J. 37, 74–86.

[Tomadakis and Sotirchos(1991b)] Tomadakis, M. M., Sotirchos, S. V., 1991b. Knudsen diffusivities and properties of structures of unidirectional fibers. AIChE J. 37, 1175–1186.

[Vaidyaraman et al.(1996)] Vaidyaraman, S., Lackey, W. J., Agrawal, P. K., Starr, T. L., 1996. 1-d model for forced-flow -thermal gradient chemical vapor infiltration process for carbon/carbon composites. Carbon 34 (9), 1123–1133.

[Vignoles et al.(2005)] Vignoles, G. L., Nadeau, N., Brauner, C.-M., Lines, J.-F., Puiggali, J.-R., 2005. The notion of densification front in CVI with thermal gradients. In: Proc. 29^{th} Intl. Conf. on Advanced Ceramics and Composites. Ceram. Eng. and Sci. Proc. The American Ceramic Society.

List of symbols

Latin

Symbol	Definition and unit
c	specific heat, $J.kg^{-1}.K^{-1}$
D	mass diffusion coefficient, $m^2.s^{-1}$
E_a	activation energy, $J.mol^{-1}$
g	gravity, $m.s^{-2}$
h	heat transfer coefficient, $W.m^{-2}.K^{-1}$
J	diffusive flux, $mol.m^{-2}.s^{-1}$
K	permeability, m^2
k_0	rate constant , $m.K^{-\beta}.s^{-1}$
p	partial pressure, Pa
q_{th}	volumetric heating power, $W.m^{-3}$
$\mathcal{R}$	perfect gas constant, $J.mol^{-1}.K^{-1}$
R	precursor consumption rate, $mol.m^{-3}.s^{-1}$
t	time, s
T	temperature, K
V	electric potential, V
V_m	deposit molar volume, $m^3.mol^{-1}$

Greek

Symbol	Definition and unit
β	chemical reaction rate coefficient (-)
ε	porosity (-)
λ	thermal conductivity, $W.m^{-1}.K^{-1}$
μ	viscosity, $Pa.s$
ρ	density, $kg.m^{-3}$
σ_e	electrical conductivity, $\Omega^{-1}.m^{-1}$
σ_v	internal surface area, m^{-1}
Φ	Thiele modulus (-)

Subscripts and underscripts

Symbol	Definition and unit
$\cdot_0$	initial state
$\cdot_b$	binary diffusion
$\cdot_c$	cyclohexane
$\cdot_{eb}$	boiling
$\cdot_g$	gas
$\cdot_K$	Knudsen diffusion
$\cdot_l$	liquid
$\cdot_r$	radial component
$\cdot_s$	solid (carbon)
$\cdot_v$	vapor
$\cdot_x$	species X ($C_{1.6}H_{4.07}$)
$\cdot_z$	axial component
$\cdot^*$	effective property

Figure captions

after 1 hour processing.

Figure 17. Sensitivity to the surface area scale factor : effect on densification profiles after 1 hour processing.

Figure 18. Influence of mass transport terms on computed densification profile after 1 hour processing.

Figure 19. Sensitivity to the magnitude of mass transport : effect on densification profile after 1 hour processing.

Figure 20. Different regimes of densification : Deposited mass after 5 h processing and maximal residual porosity as a function of the external imposed temperature.

Figure 21. Typical porosity profiles in the three identified densification regimes.

Figure 22. Local heat flux, front velocity and width during a typical run.

Table captions

- Table 1. Balance equations and constitutive laws.
- Table 2. List of chosen preform properties for model validation.
- Table 3. List of chosen composite properties for model validation.
- Table 4. Densification parameters for model validation.
- Table 5. Mass transfer parameters for model validation.
- Table 6. List of process parameters for model validation.
- Table 7. Sensitivity to solid-phase thermal conductivity : effect on various indicators at $t = 1$ hour.
- Table 8. Various laws for internal surface area.
- Table 9. Sensitivity to surface area laws : effect on various indicators at $t = 1$ hour.

Tables

Subset	Balance equations	Constitutive laws
Resistive heating	$\nabla \cdot (\sigma_e^* \underline{\nabla} V) = 0$	$\sigma_e^* = f(T, \varepsilon)$
Heat transfer	$(\rho c)^* \dfrac{\partial T}{\partial t} + \nabla \cdot \left(-\underline{\underline{\lambda^*}} \cdot \underline{\nabla} T\right) =$ $q_{th} - R\Delta_r H(T)$	$\rho c^*, \lambda^* = f\left(T, \varepsilon\right)$ $q_{th} = \dfrac{1}{2}\dfrac{1}{\sigma_e}\left\|\sigma_e \underline{\nabla} V\right\|^2$
Chemical reaction	$C_6H_{12}(g) \rightarrow$ $1.29\,\mathrm{pyC}(s) + 2.95\,\mathrm{C}_{1.6}H_{4.07}(g)$	$R = \sigma_v\left(\varepsilon\right) k_0 T^{\beta} \left(\dfrac{p_c}{\mathcal{R}T}\right) \exp\left(-\dfrac{E_a}{\mathcal{R}T}\right)$
Species	$\dfrac{\partial}{\partial t}\left(\dfrac{\varepsilon p_c}{\mathcal{R}T}\right) + \nabla \cdot \underline{J_c} + R = 0$ $\dfrac{\partial}{\partial t}\left(\dfrac{\varepsilon p_x}{\mathcal{R}T}\right) + \nabla \cdot \underline{J_x} - 2.95R = 0$	
Fluxes	$J_c = \left[-\frac{x_c D_{c,K} D_{x,K} + D_{c,K} D_{cx}}{x_c D_{x,K} + D_{cx} + x_x D_{c,K}} \frac{\nabla p_c}{\mathcal{R}T} - \frac{x_c D_{c,K} D_{x,K}}{x_x D_{x,K} + D_{cx} + x_x D_{c,K}} \frac{\nabla p_x}{\mathcal{R}T}\right] - \frac{p_c}{\mathcal{R}T}\frac{K}{\mu^*}\nabla p$ $J_x = \left[-\frac{x_x D_{c,K} D_{x,K}}{x_c D_{x,K} + D_{cx} + x_x D_{c,K}} \frac{\nabla p_c}{\mathcal{R}T} - \frac{x_x D_{c,K} D_{x,K} + D_{x,K} D_{cx}}{x_c D_{x,K} + D_{cx} + x_x D_{c,K}} \frac{\nabla p_x}{\mathcal{R}T}\right] - \frac{p_x}{\mathcal{R}T}\frac{K}{\mu^*}\nabla p$	
Densification	$\dfrac{\partial \varepsilon}{\partial t} = 1.29 R V_m$	

Table 1

Balance equations and constitutive laws

Parameter	Value	Unit
Preform properties		
Initial open porosity	$\varepsilon_0 = 0.94$	-
Initial fiber diameter	$d_{f0} = 10 \cdot 10^{-6}$	m
Fiber density	$\rho_f = 1440$	$kg.m^{-3}$
Deposit density	$\rho_d = 2180$	$kg.m^{-3}$
Total density	$\rho(\varepsilon) = (1-\varepsilon_0)\rho_f + (\varepsilon_0 - \varepsilon)\rho_d + \varepsilon\rho_g$	
Internal surface area	$\sigma_v = \frac{4}{d_f}\left[(2-\varepsilon_0)\left(\frac{\varepsilon}{\varepsilon_0}\right) - \left(\frac{\varepsilon}{\varepsilon_0}\right)^2\right]$	m^{-1}
Effective pore diameter	$d_p(\varepsilon) = 4\frac{\varepsilon}{\sigma_v}$	m
Tortuosities for		
Ordinary diffusion	$\eta_d(\varepsilon) = \varepsilon^{-2/3}$	-
[Sotirchos and Tomadakis(1990)]		
Knudsen diffusion	$\eta_K(\varepsilon) = 1.444\varepsilon^{-1}$	-
[Sotirchos and Tomadakis(1990)]		
Viscous transport	$\eta_v(\varepsilon) = 2.76\varepsilon^{-2/3}(\ln\varepsilon)^2$	-
[Tomadakis and Robertson(2005)]		

Table 2

List of chosen preform properties for model validation.

Parameter	Value	Unit
	Composite (gas+preform) properties	
Electrical conductivity	$\sigma_\theta(\varepsilon) = (1-\varepsilon)\sigma_s$	
	$\sigma_s = 25000$	$\Omega^{-1}.m^{-1}$
Specific heat	$(\rho c)^*(\varepsilon, T) = (1-\varepsilon_0)\rho_f c_f + (\varepsilon_0 - \varepsilon)\rho_d c_d + \varepsilon \rho_g c_g$	$J.kg^{-1}.K^{-1}$
	$c_f(T) = c_d(T) = -42.4678 + 2.8516\,T - 0.001\,T^2$	
	$c_g(T) = -649.29 + 7.28\,T - 0.003\;T^2 + 1.57 \cdot 10^{-7}\;T^3$	
Thermal conductivity	$\lambda^*(\varepsilon, T, p) = (1-\varepsilon_0)\lambda_f + (\varepsilon_0 - \varepsilon)\lambda_d + \varepsilon\lambda_g$	$W.m^{-1}.K^{-1}$
	$\lambda_f(T) = 1.1176 - 6.217 \cdot 10^{-4}\,T + 8.3 \cdot 10^{-7}\,T^2$	
	$\lambda_d(T) = -3.466 + 0.0271\,T - 2.05 \cdot 10^{-5}\,T^2 + 5.3 \cdot 10^{-9}\,T^3$	
	$\lambda_g(T, \varepsilon, p)^{-1} = \lambda_{gl}(T)^{-1} + (d_p(\varepsilon)p)^{-1}\sqrt{\frac{\pi M_{12} T}{2\mathcal{R}}}$	
	$\lambda_{gl}(T) = -0.02329 + 1.1092 \cdot 10^{-4}\,T - 2.0 \cdot 10^{-8}\;T^2$	

Table 3

List of chosen composite properties for model validation.

Parameter	Value	Unit
Densification parameters		
Chemical deposition	$k_0 = 8.0$	$m.s^{-1}.K^{-\beta}$
rate	$\beta = 2.02$	-
	$E_a = 305 \cdot 10^3$	$J.mol^{-1}$
Deposit molar volume	$V_m = 5.5 \cdot 10^{-6}$	$m^3.mol^{-1}$

Table 4

Densification parameters for model validation.

Parameter	Value	Unit
	Mass Transfer parameters	
Darcy Permeability	$K(\varepsilon) = \varepsilon \dfrac{d_p^2}{32\eta_v}$	m^2
Gas Viscosity	$\mu^*(T) = 10^{-7}\left(-9.61 + 0.358T - 1.46 \cdot 10^{-4}T^2 + 3.63 \cdot 10^{-8}T^3\right)$	$Pa.s$
Diffusivity (ordinary)	$D_{cx}(\varepsilon, T, p) = \dfrac{\varepsilon}{\eta_b} \dfrac{2.62 \cdot 10^{-8} T^{3/2}}{p\sqrt{M_{12}}\sigma_{12}^2 \Omega_d}$	$m^2.s^{-1}$
Diffusivity (Knudsen)	$D_{i,K}(\varepsilon, T) = \dfrac{1}{3}\dfrac{\varepsilon}{\eta_K}\sqrt{\dfrac{8 \cdot \mathcal{R}T}{\pi M_i}} \cdot d_p$	$m^2.s^{-1}$

Table 5

Mass transfer parameters for model validation

Parameter	Value
Reactor and preform dimensions	
Resistor internal radius	$r_i = 8.0 \cdot 10^{-3}\ m$
Resistor external radius	$r_i = 1.0 \cdot 10^{-2}\ m$
Preform external radius	$r_i = 2.5 \cdot 10^{-2}\ m$
Sample height	$h = 9.0 \cdot 10^{-2}\ m$
Reactor and preform parameters	
Total pressure	$P_{tot} = 1.013 \cdot 10^5\ \ Pa$
Inner wall	
temperature	$T = 1373\ K$
Outer wall	
temperature	$T_{eb}(C_6H_{12}) = 378\ K$
Heat transfer coefficient	$h = 200\ W.m^2.K^{-1}$

Table 6

List of process parameters for model validation

Case	Front position (mm)	Front width (mm)	Power (W)
Base	5.4	4.6	683
Double λ_s	6.1 (+13.0%)	5.3 (+15.2%)	1199 (+75.6%)
Half λ_s	4.9 (−9.3%)	4.0 (−13.0%)	381 (−44.3%)

Table 7

Sensitivity to solid-phase thermal conductivity : effect on various indicators at $t = 1$ hour.

Law ♯	Expression	Comment
1	$\sigma_v = \frac{4}{d_f}\left[(2-\varepsilon_0)\left(\frac{\varepsilon}{\varepsilon_0}\right) - \left(\frac{\varepsilon}{\varepsilon_0}\right)^2\right]$	Polynomial
2	$\sigma_v = -\frac{4}{d_f}\varepsilon \ln \varepsilon$	Random cylinders [Tomadakis and Sotirchos(1991a)]
3	$\sigma_v = \frac{4}{d_f}\frac{\varepsilon}{\varepsilon_0}(1-\varepsilon)\left(\varepsilon_0^{-1}\ln\left(\frac{\varepsilon_0}{\varepsilon}\right)+1\right)$	Random cylinders with hard-core porosity (adapted from [Rikvold and Stell(1985)])
4	$\sigma_v = \frac{4}{d_f}\left[\left(2-\frac{3}{2}\varepsilon_0\right)\left(\frac{\varepsilon}{\varepsilon_0}\right) - \left(1-\frac{\varepsilon_0}{2}\right)\left(\frac{\varepsilon}{\varepsilon_0}\right)^2\right]$	Polynomial with half slope at ε_0
5	$\sigma_v = \frac{4}{d_f}(1-\varepsilon)\frac{\left(-\frac{3}{4\pi}\ln(1-\varepsilon)\right)^{2/3}+\varepsilon}{\left(-\frac{3}{4\pi}\ln(1-\varepsilon_0)\right)^{2/3}+\varepsilon_0}$	Interpolation between spherical pores at small ε and isolated cylinders at high ε

Table 8

Various laws for internal surface area.

Case	Front position (mm)	Front width (mm)	Power (W)	Scaled Average $\overline{\sigma}_v.d_f$
Law ♯1 (Base)	5.39	6.86	683	0.793
Law ♯2	4.66 (−13.5%)	3.38 (−50.7%)	632 (−7.5%)	1.047 (+32.0%)
Law ♯3	4.91 (−9.0%)	2.96 (−56.8%)	642 (−6.0%)	1.349 (+70.1%)
Law ♯4	4.34 (−19.5%)	7.69 (+12.1%)	625 (−8.4%)	0.335 (−57.8%)
Law ♯5	4.26 (−21.0%)	5.38 (−21.5%)	626 (−8.3%)	0.702 (−11.5%)
Law ♯1	5.39	6.86	683	0.793
Half Law ♯1	3.57 (−33.8%)	6.80 (−0.9%)	575 (−15.8%)	0.396 (−50%)
Double Law ♯1	7.21 (+33.8%)	6.44 (−6.1%)	816 (+19.4%)	1.586 (+50%)

Table 9

Sensitivity to surface area laws : effect on various indicators at $t = 1$ hour.

Figures

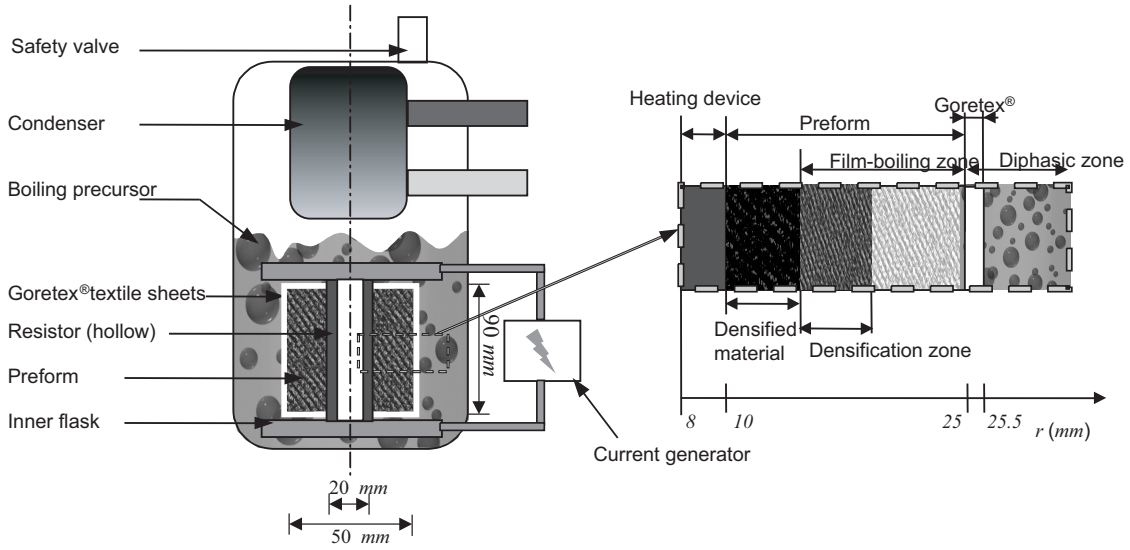

Fig. 1. Descriptive scheme of the rapid densification process.

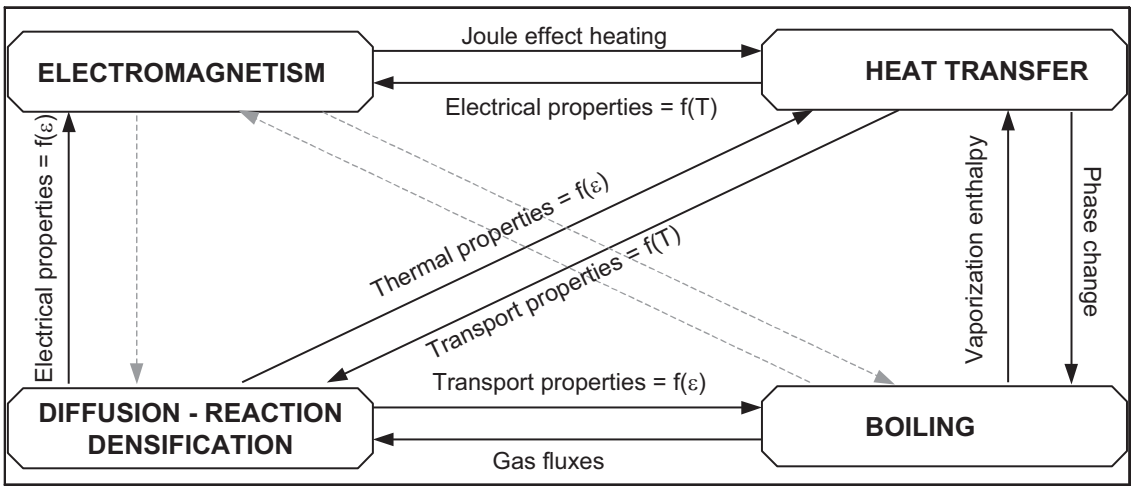

Fig. 2. Couplings between the different phenomena subsets.

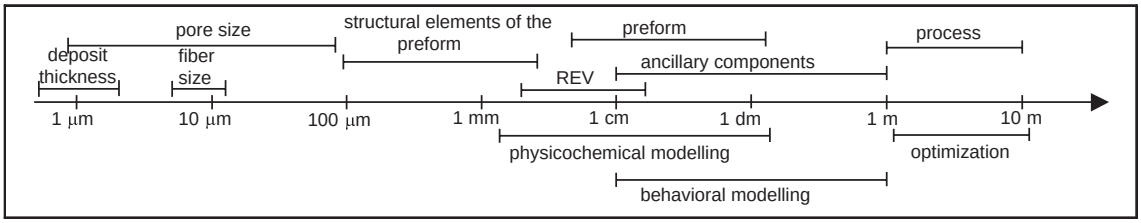

Fig. 3. Characteristic length scales for the process elements.

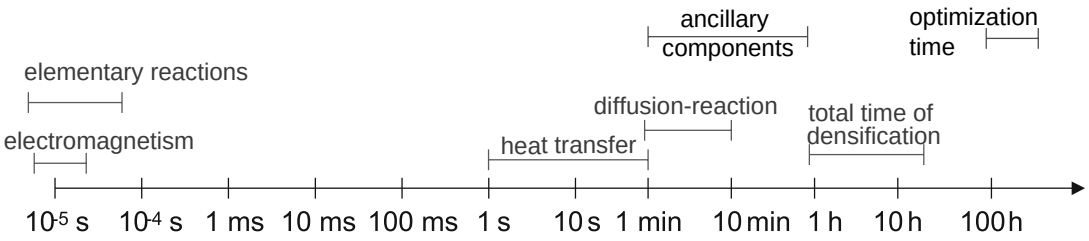

Fig. 4. Characteristic time scales for the process elements.

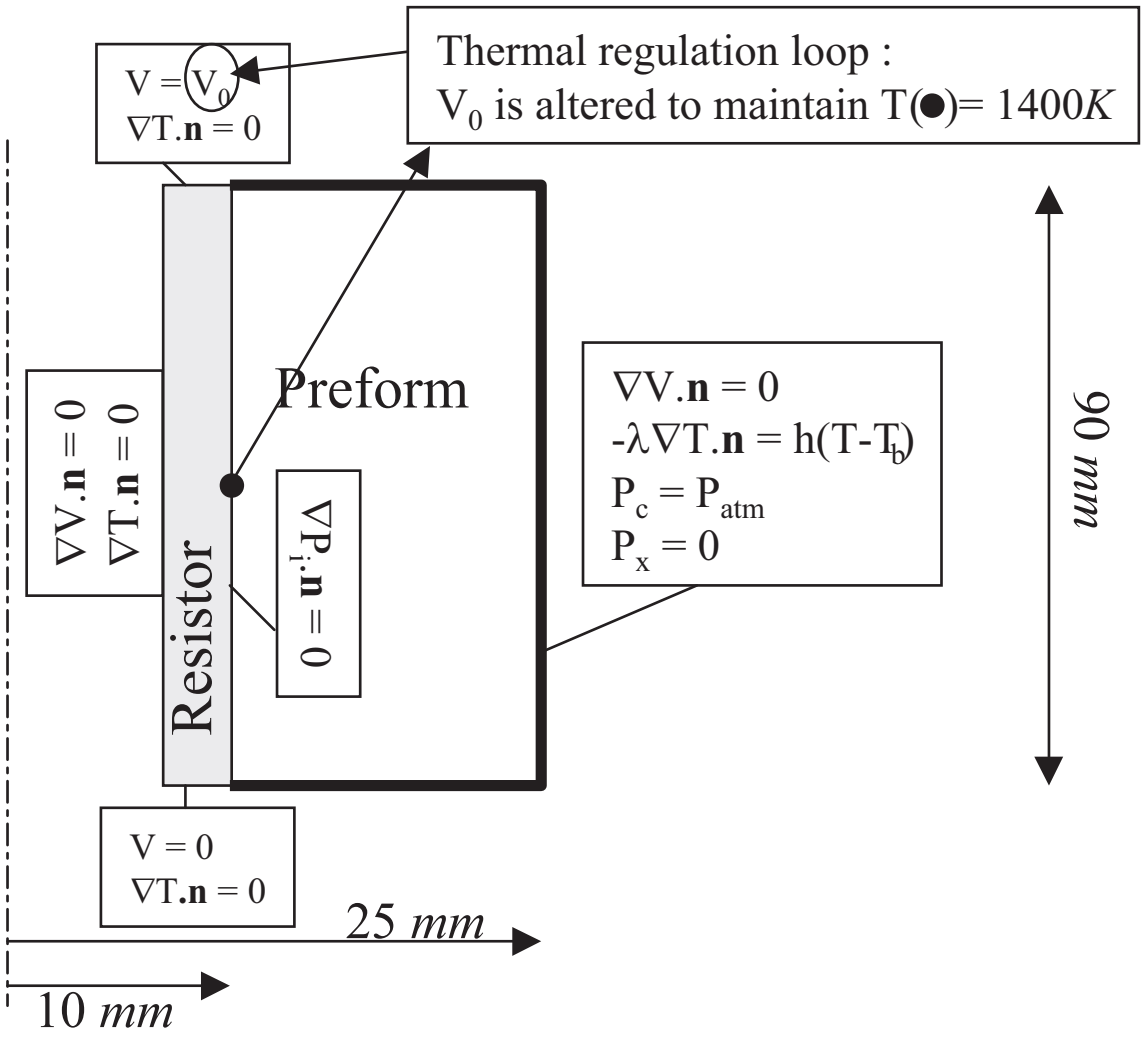

Fig. 5. Computational domain and boundary conditions.

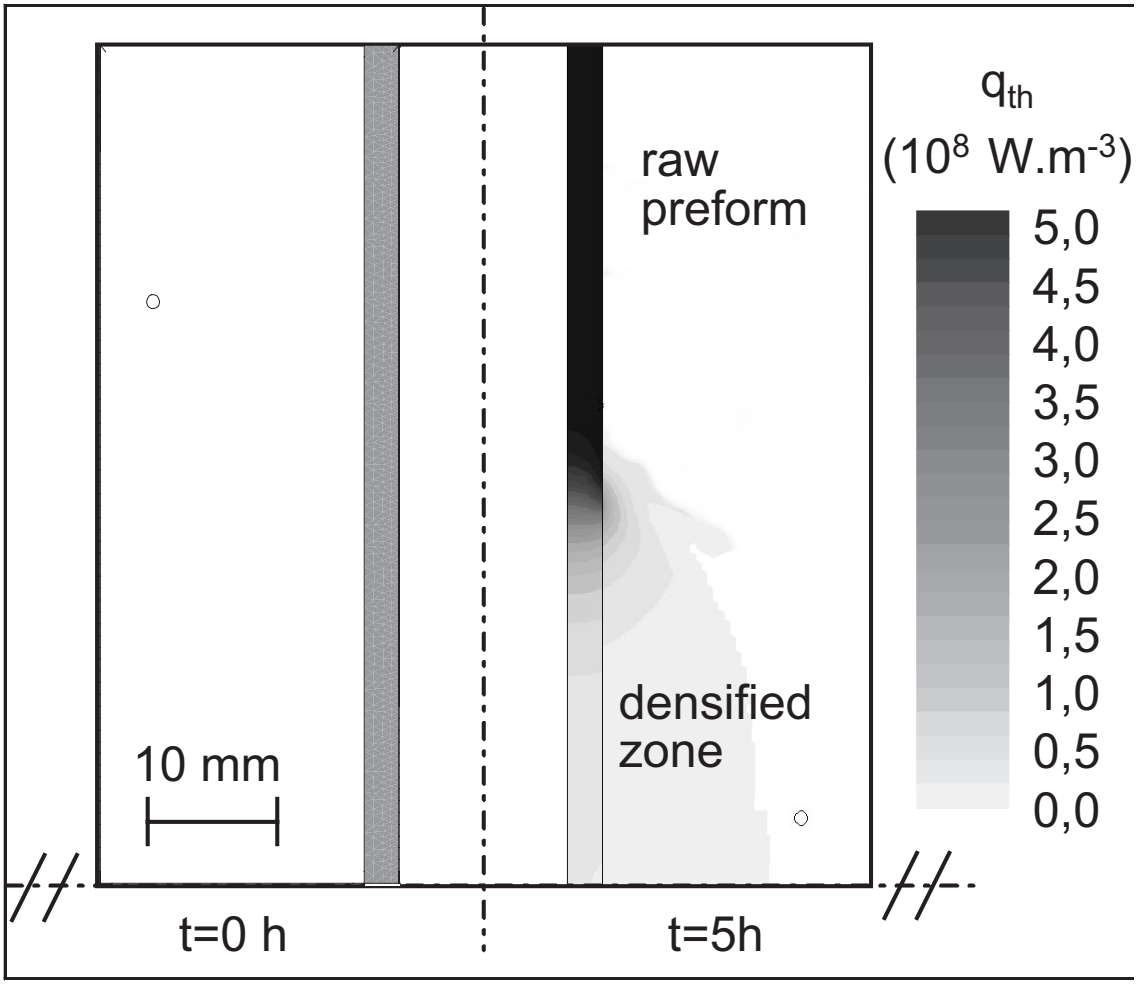

Fig. 6. Joule heating power field inside the upper halves of the resistor and preform at the beginning (left) and the end (right) of densification.

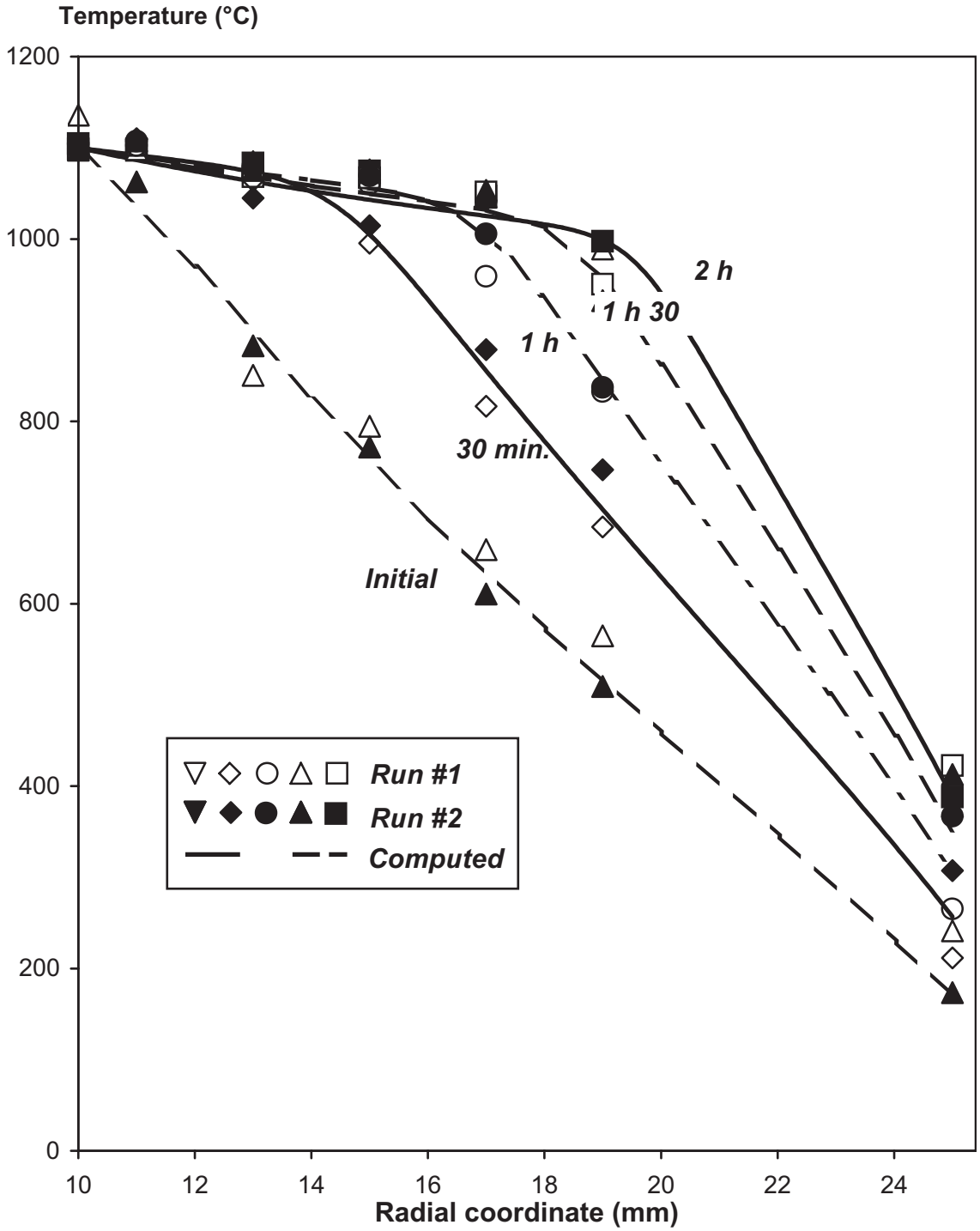

Fig. 7. Comparison between numerical and experimental radial thermal profiles at preform half-height. The filled and open symbols are related to two different runs, and the lines are computed values.

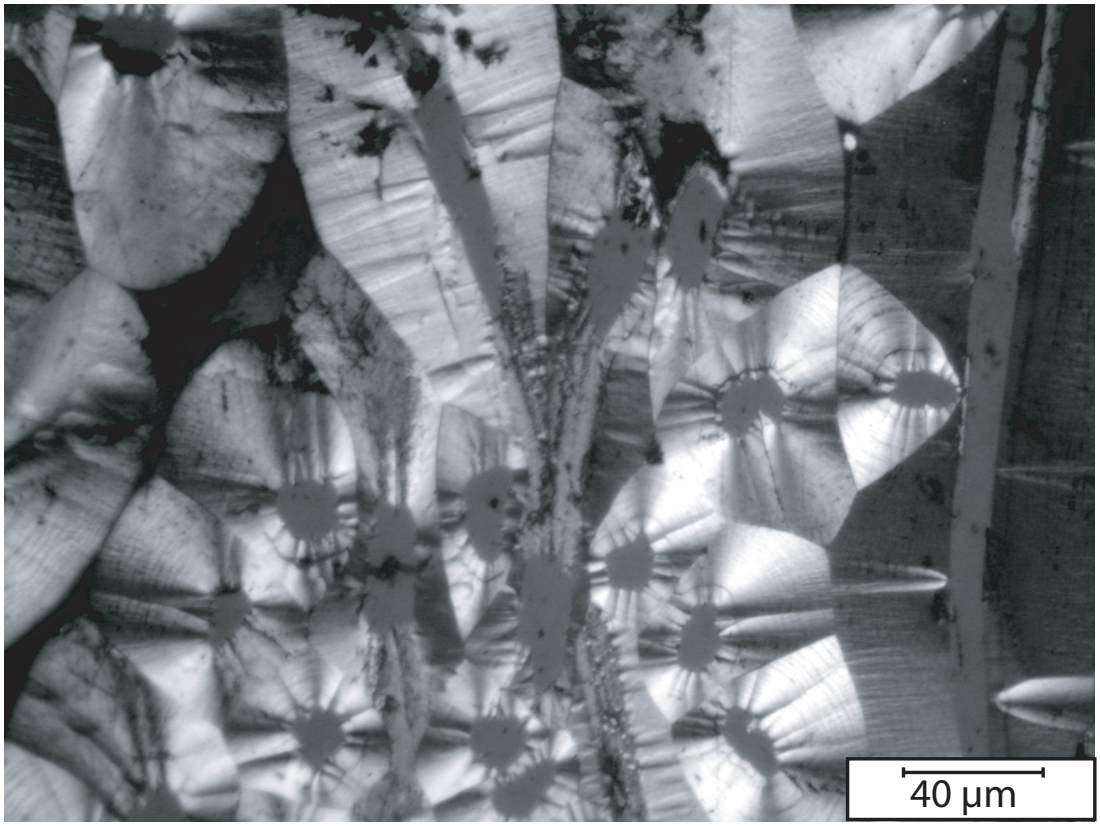
40 µm

a)

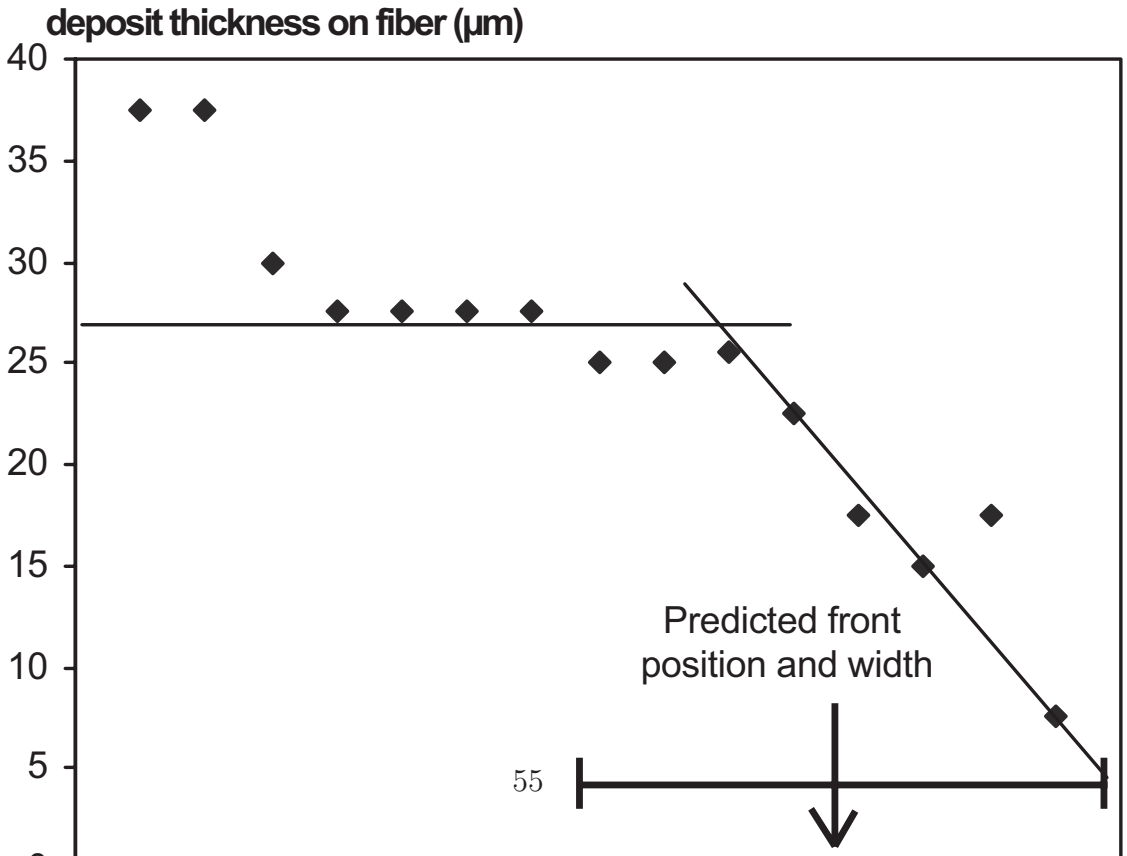
deposit thickness on fiber (µm)
40
35
30
25
20
15
10
5
Predicted front
position and width

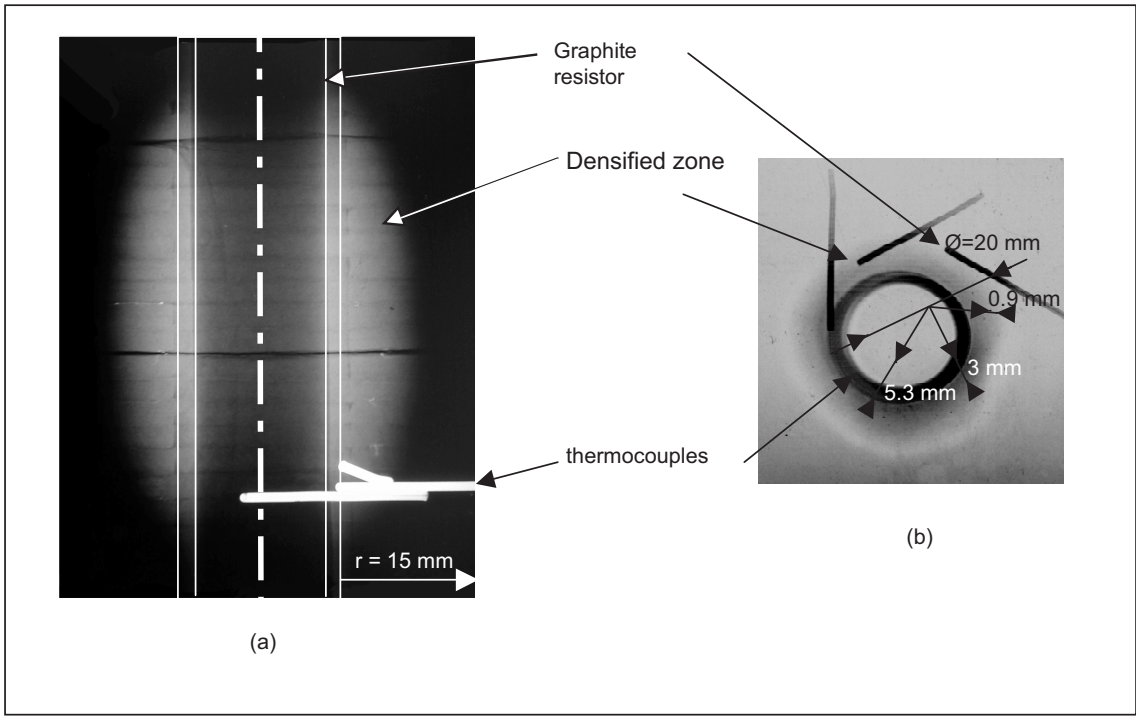

Fig. 9. Assessment of the position of thermocouples using X-ray radiographs. (a) Axial position with horizontal projection, (b) radial position with vertical projection.

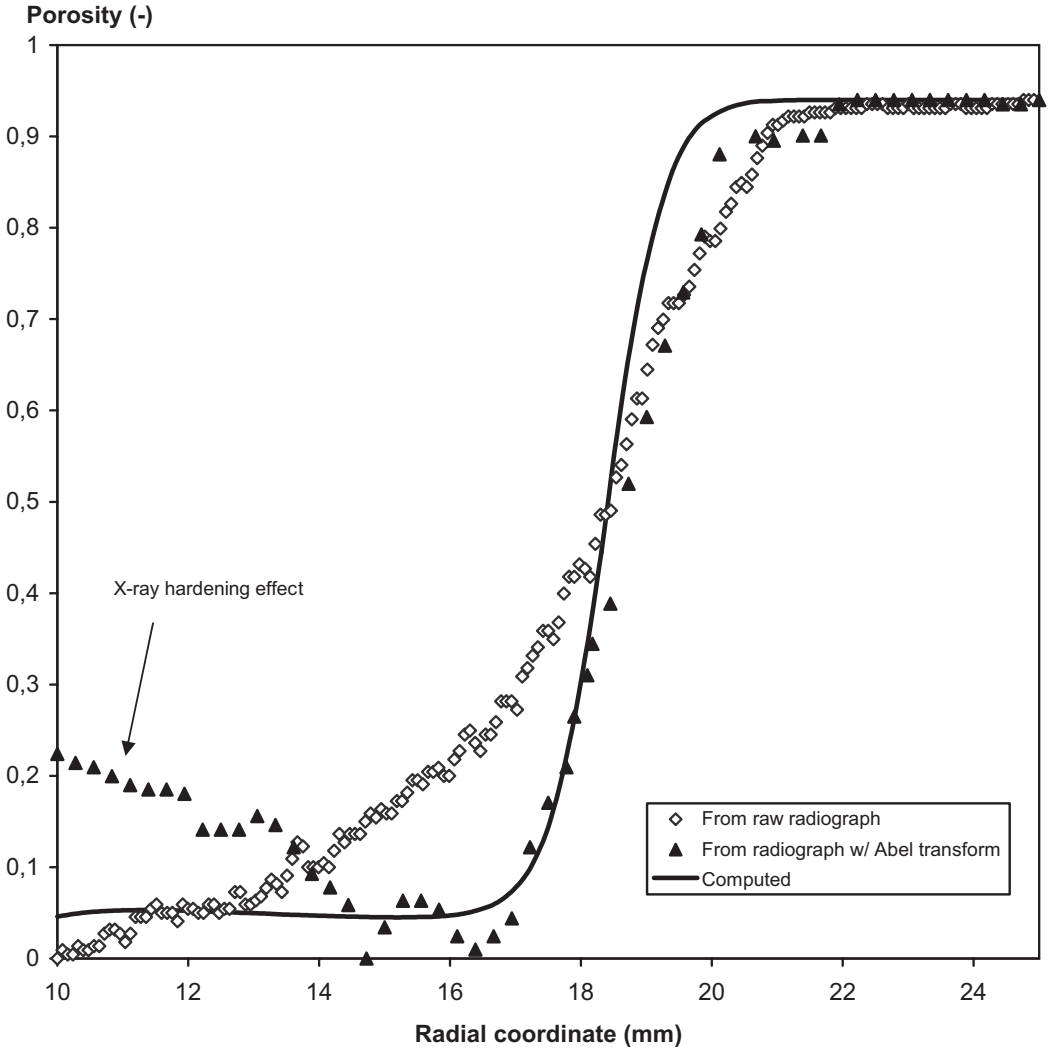

Fig. 10. Comparison of computed and measured centerline radial density profiles using X-ray radiographs and Abel transform, after 2 hours processing.

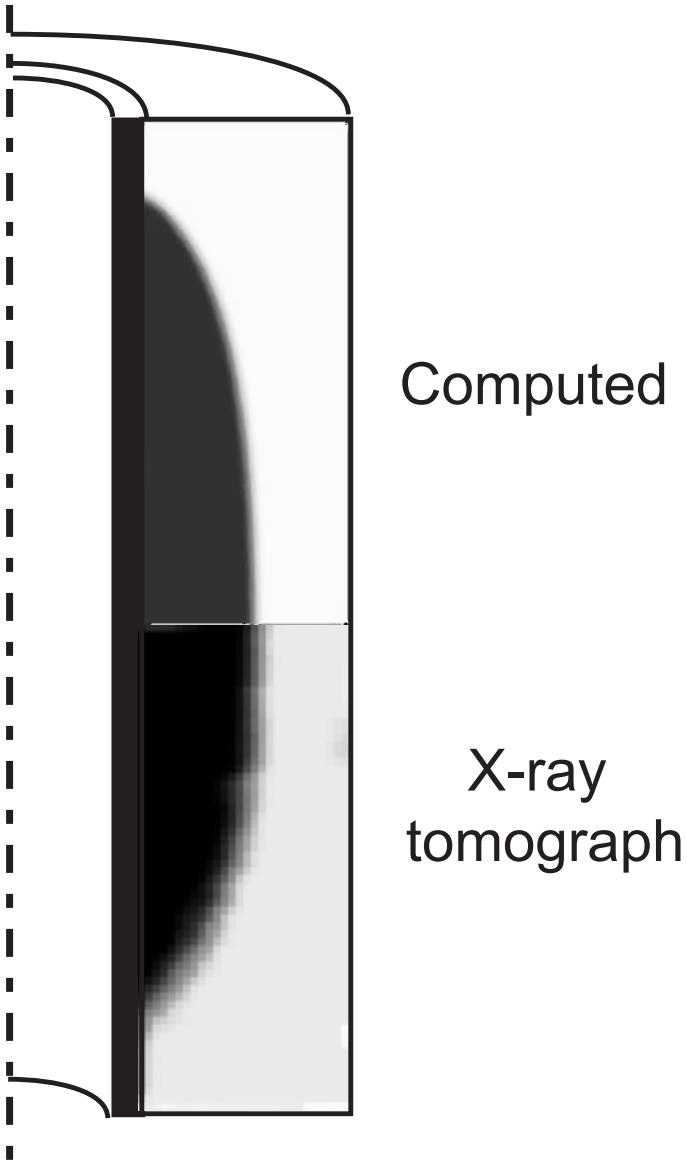

Fig. 11. Comparison of computed and measured density profiles using X-ray Computerized Tomography, after 2 hours processing.

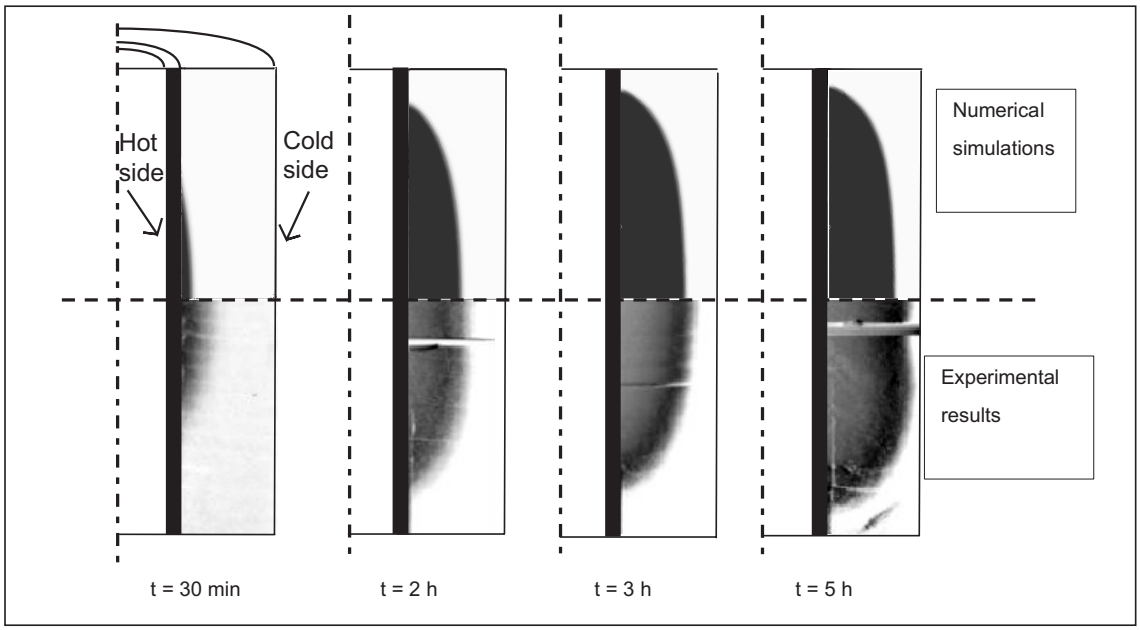

Fig. 12. Comparison of computed and measured density profiles using X-ray radiographs and Abel transform.

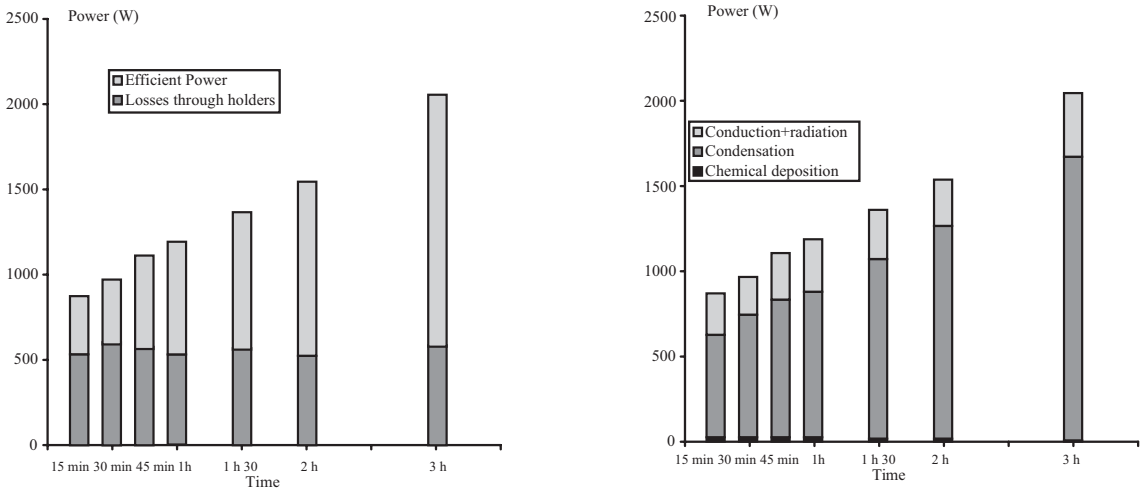

Fig. 13. Time evolution of power. Left : input power ; right : output power.

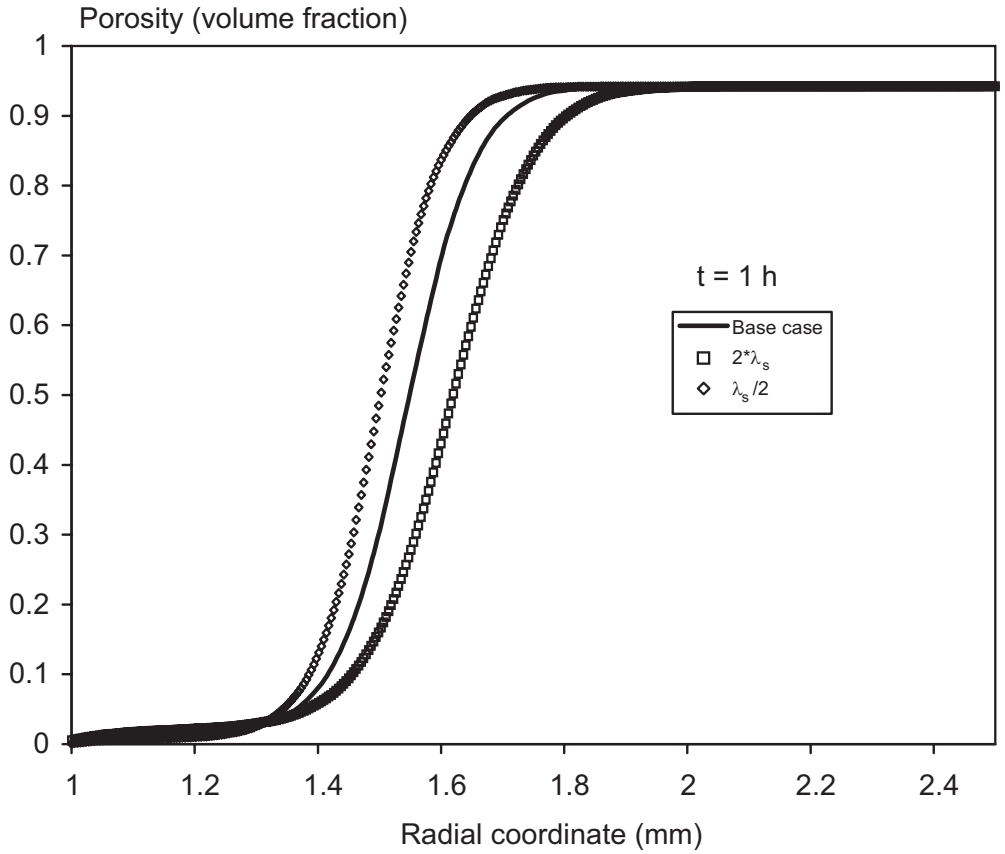

Fig. 14. Sensitivity to the thermal conductivity : effect on density profiles after 2 hours.

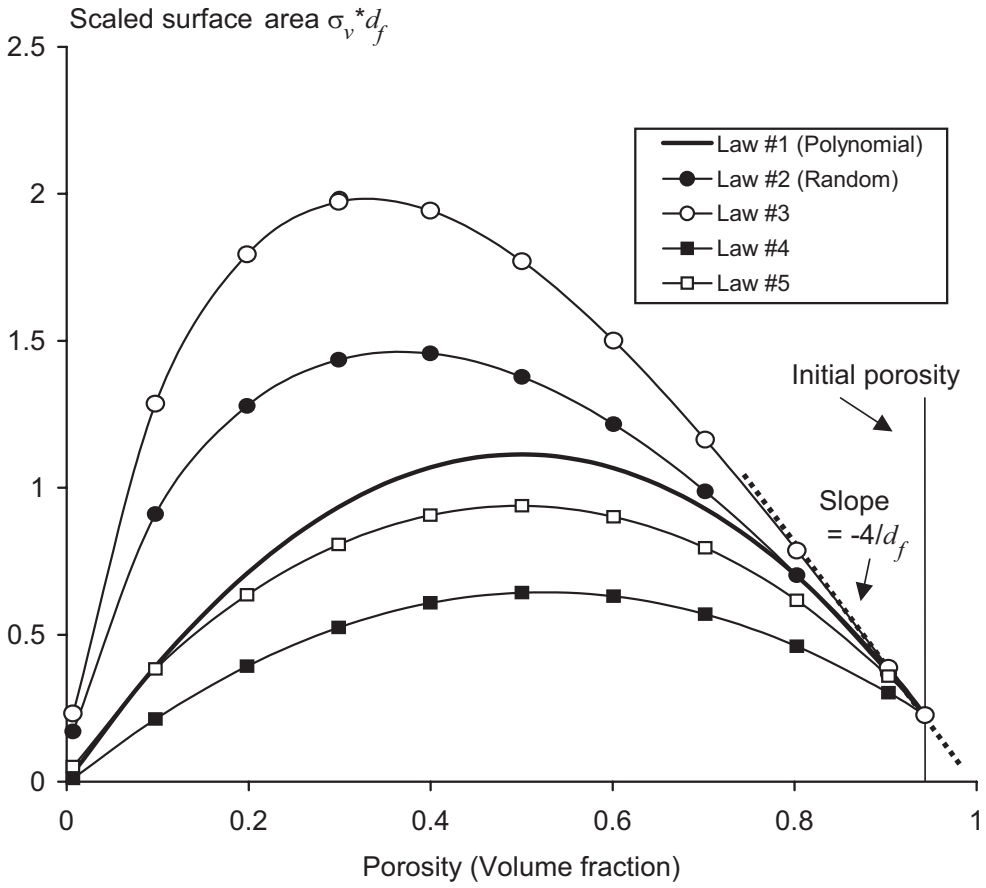

Fig. 15. Several laws for surface area as a function of total porosity.

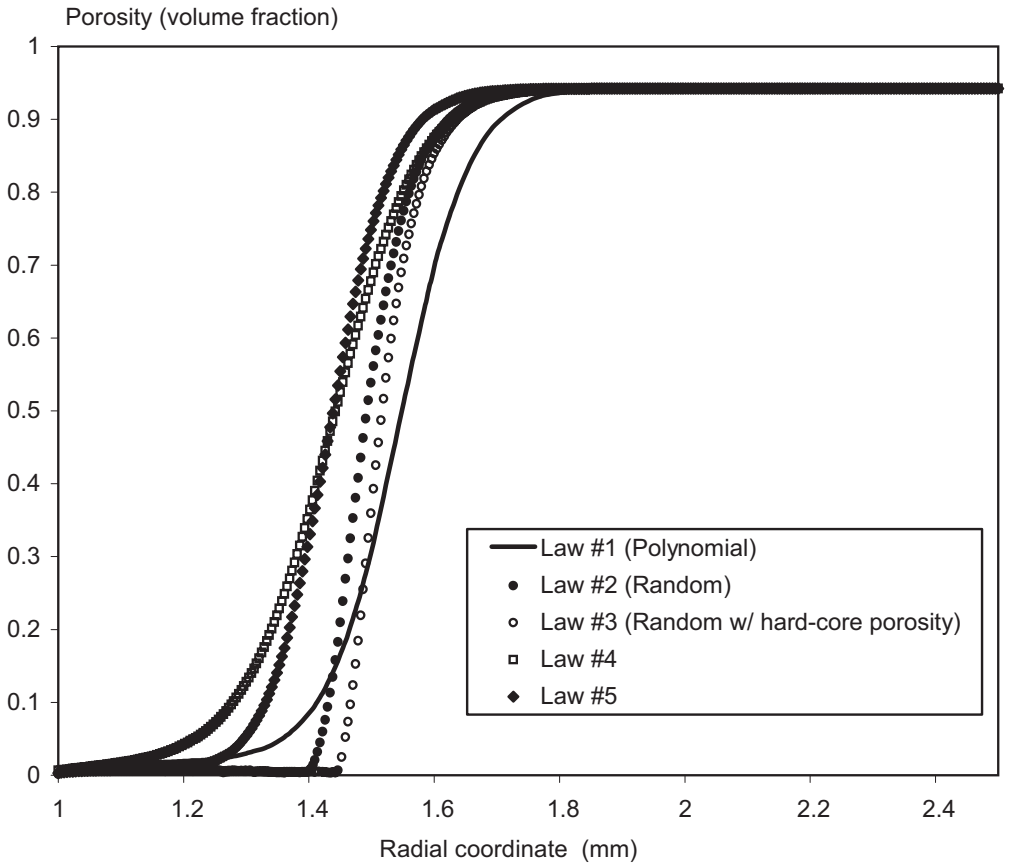

Fig. 16. Sensitivity to the surface area laws : effect on densification profiles after 1 hour processing.

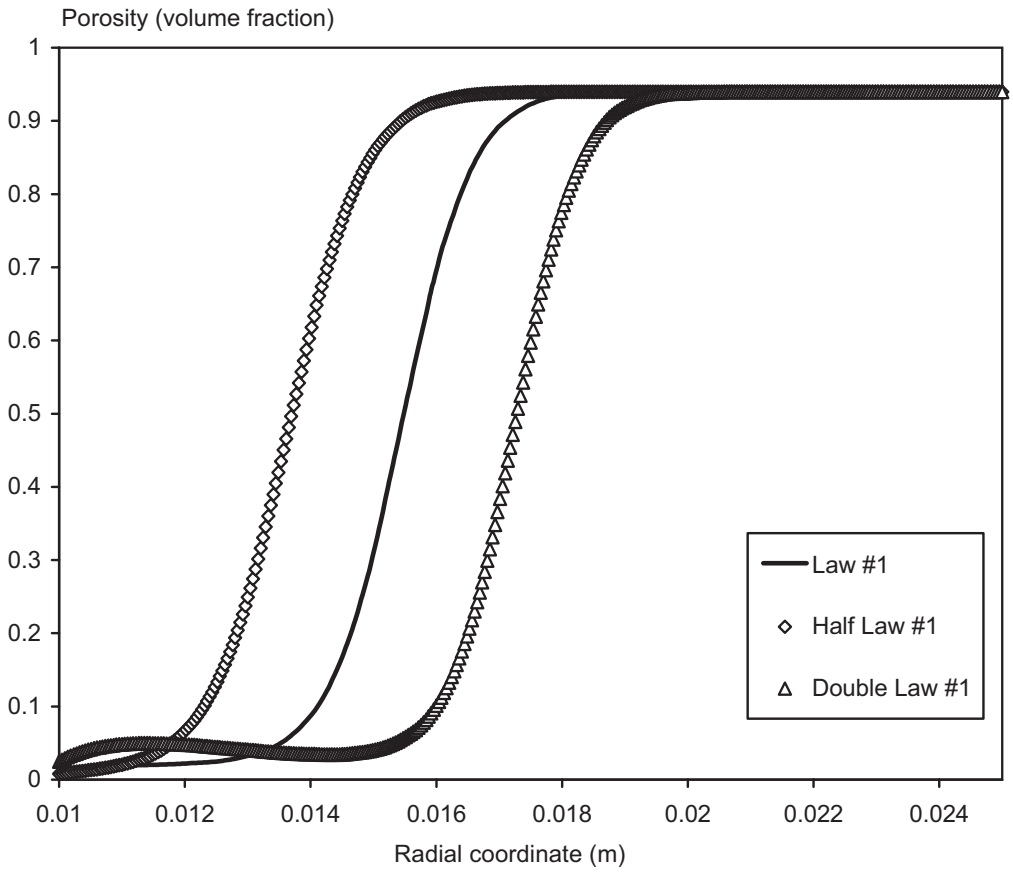

Fig. 17. Sensitivity to the surface area scale factor : effect on densification profiles after 1 hour processing.

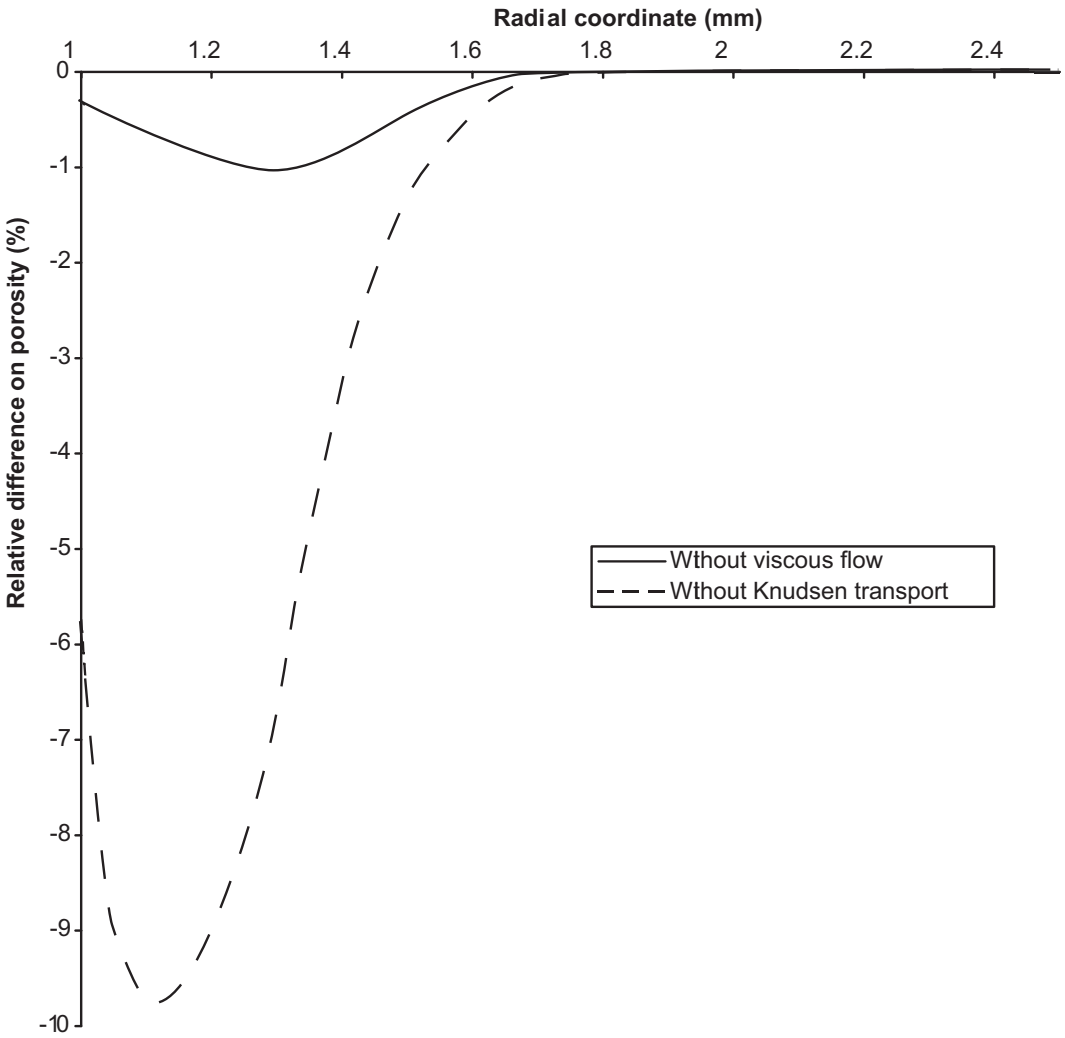

Fig. 18. Influence of mass transport terms on computed densification profile after 1 hour processing.

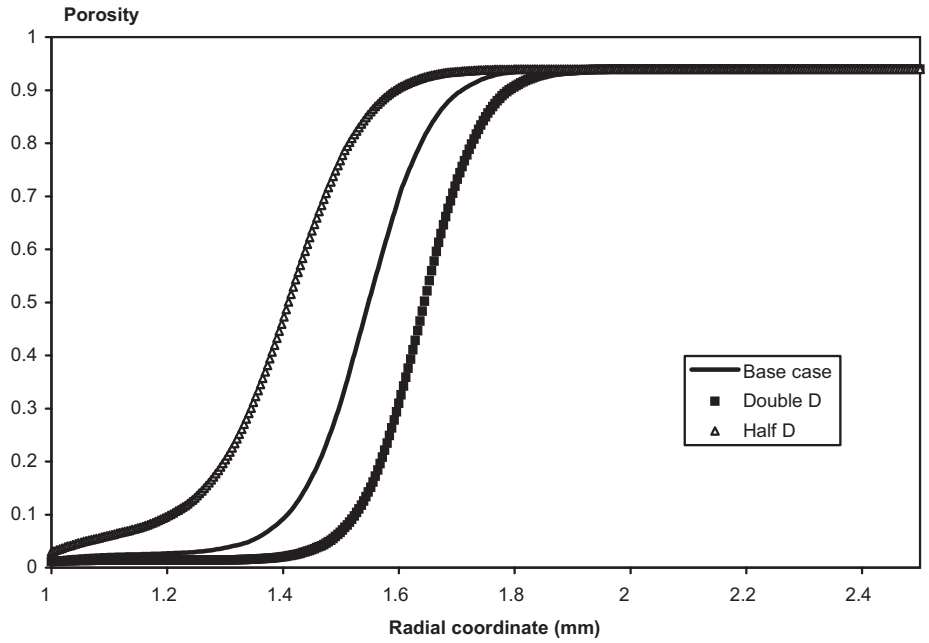

Fig. 19. Sensitivity to the magnitude of mass transport : effect on densification profile after 1 hour processing.

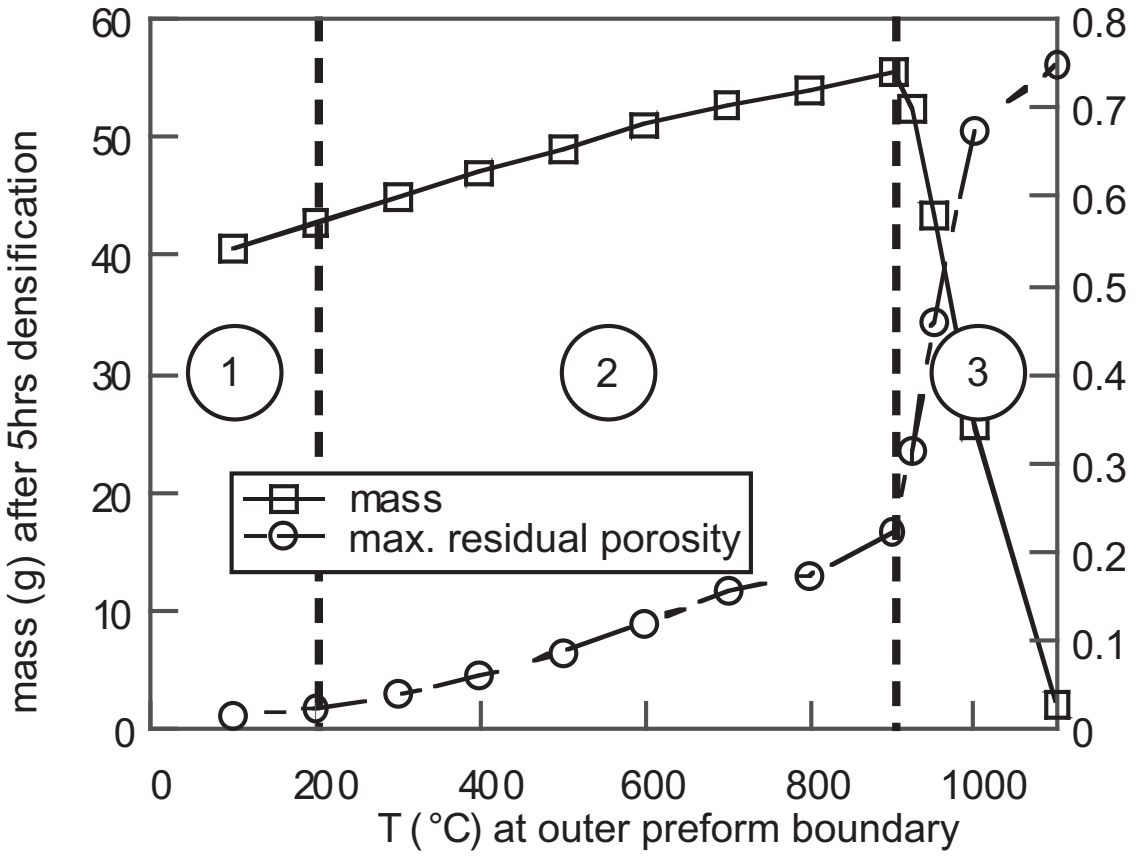

Fig. 20. Different regimes of densification : Deposited mass after 5 h processing and maximal residual porosity as a function of the external imposed temperature.

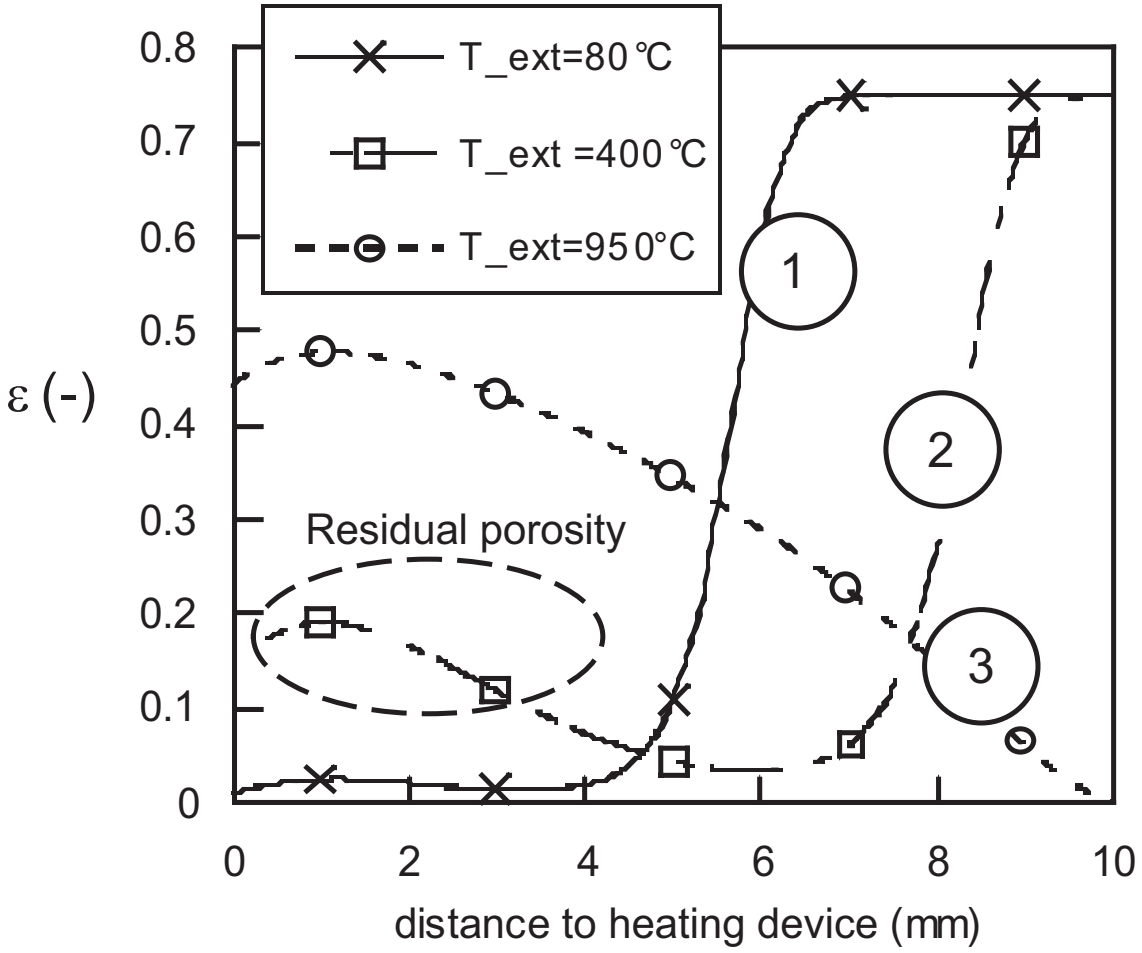

Fig. 21. Typical porosity profiles in the three identified densification regimes.

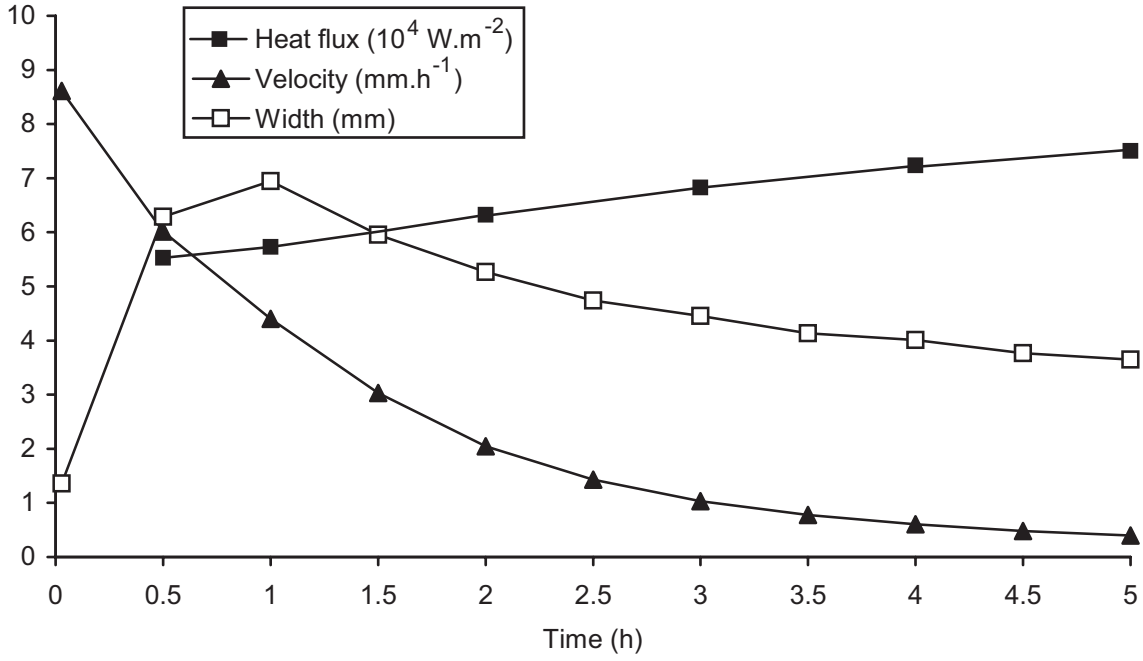

Fig. 22. Local heat flux, front velocity and width during a typical run.